J. Fluid Mech. (2001), *vol.* 434, *pp.* 65–100. Printed in the United Kingdom

Annular and spiral patterns in flows between rotating and stationary discs

By E. SERRE[1], E. CRESPO DEL ARCO[2] AND P. BONTOUX[1]

[1]Dpt. Modélisation Numérique, LABM UMSR 2164 CNRS/IRPHE UMR 6594
CNRS/Université d'Aix-Marseille II, La Jetée-IMT Château-Gombert,
38 rue Frédéric Joliot-Curie, 13451 Marseille cedex 20, France

[2]UNED, Dpto. Fisica Fundamental, Apdo. 60.141, 28080 Madrid, Spain

(Received 30 June 1999 and in revised form 20 October 2000)

Different instabilities of the boundary layer flows that appear in the cavity between stationary and rotating discs are investigated using three-dimensional direct numerical simulations. The influence of curvature and confinement is studied using two geometrical configurations: (i) a cylindrical cavity including the rotation axis and (ii) an annular cavity radially confined by a shaft and a shroud. The numerical computations are based on a pseudo-spectral Chebyshev–Fourier method for solving the incompressible Navier–Stokes equations written in primitive variables. The high level accuracy of the spectral methods is imperative for the investigation of such instability structures. The basic flow is steady and of the Batchelor type. At a critical rotation rate, stationary axisymmetric and/or three-dimensional structures appear in the Bödewadt and Ekman layers while at higher rotation rates a second transition to unsteady flow is observed. All features of the transitions are documented. A comparison of the wavenumbers, frequencies, and phase velocities of the instabilities with available theoretical and experimental results shows that both type II (or A) and type I (or B) instabilities appear, depending on flow and geometric control parameters. Interesting patterns exhibiting the coexistence of circular and spiral waves are found under certain conditions.

1. Introduction

The study of rotating viscous flow near stationary or rotating discs has significant relevance to many industrial devices. Early experimental (Faller 1963) and theoretical (Hide 1968) studies of the fluid motion near a rotating disc were carried out to better understand flows in the atmosphere and oceans. The stable boundary layer flows and the first nonlinear regimes were then identified and partially characterized. This problem is also of considerable fundamental interest (see Hide 1968; Greenspan 1969). Industrial applications have motivated studies involving more complex geometries, often with throughflow and heat transfer. Fundamental investigations that are relevant to the cooling of gas turbines and turbomachinery are reported in a series of papers by Owen & Rogers (1989, 1995). Typical configurations are cavities between rotating compressors or turbine discs, between counter-rotating discs, and in a rotor–stator system with or without throughflow. A characteristic of these flows is the coexistence of adjacent and coupled flow regions that are radically different in terms of the flow properties and the thickness scales of the Ekman and Bödewadt boundary layers compared to those of the geostrophic core region.

A study of the flow confined between two infinite parallel discs, one at rest and the other rotating was carried out by Batchelor (1951). His analysis showed that three flow regions develop at high rotation rate, having the structure of two shear layers near the walls bounding an inviscid core rotating at constant angular velocity. The flow is now referred to in the literature as a 'Batchelor flow'. An alternative similarity solution that does not involve a core region was proposed by Stewartson (1953) ('Stewartson flow') in the same geometry but at smaller rotation rates. However, Szeto (1978) later showed that the Batchelor flow similarity solution was the only stable one. In theoretical and experimental studies of this configuration at high Reynolds number, Daily & Nece (1960) pointed out the existence of four regimes, two stationary and two turbulent, corresponding to joined or separated boundary layers, depending on the rotation rate and geometrical parameters.

In the limit of high rotation rate, the flow between a rotating and a stationary disc presents two separated boundary layers – of Ekman type on the rotating disc and of Bödewadt type on the stationary disc – and there now exists an extensive literature on transition in these boundary layers; see Faller (1991), Greenspan (1969) and Savas (1987) for references. Two basic types of instability for corotation of the fluid and the disc have been documented both experimentally and theoretically. Historically these are referred to as type I (or type B) and type II (or type A) instabilities and both instability types have been observed when the disc is differentially rotating slower or faster than the fluid (see, for example, Weidman 1976, figure 7). The type I instability first reported by Smith (1947) arises from the presence of an inflection point in the boundary layer velocity profile. It is also referred to as a 'crossflow' instability, observed in the flow over a swept wing, where it consists of a series of standing vortices in the boundary layer (Reed & Saric 1989). The mechanism for type II instability is related to the combined effects of Coriolis and viscous forces. The spatial structure of both instabilities consists of travelling vortices in the boundary layers: their wavelength depends on the boundary layer thickness, and the orientation of their wave fronts with respect to the geostrophic flow is positive for the type I (B) instability and negative for the type II (A) instability.

Using a linear stability analysis, Lilly (1966) found that the onset of the type II instability in the Ekman layer corresponds to a lower critical Reynolds number than for type I. The critical Reynolds numbers for Ekman layers are close to $Re_{\delta c,II} \simeq 55$ and $Re_{\delta c,I} \simeq 120$ where $Re_\delta = U\delta/\nu$, U is the reference velocity of the flow outside the boundary layer and the reference length is the thickness scale of the boundary layer, $\delta = (\nu/\Omega)^{1/2}$. The values of the critical Reynolds number for Bödewadt layers over stationary discs are smaller than for Ekman layers over rotating discs: linear stability analyses by Faller (1991), Pikhtov & Smirnov (1993) report local critical values of $Re_{\delta c,I} \approx Re_{\delta c,II} \simeq 20$. Linear stability analyses of the flow between a rotating and a stationary disc, exhibiting several instabilities, have been performed by San'kov & Smirnov (1991) using similarity solutions as base flow and by Itoh (1991) who studied the stability of Batchelor type solutions with a separated boundary layer, i.e. for high values of the rotation rate. The critical values of these authors do not agree and the mechanisms of the instability are not well elucidated. A good discussion on this subject may be found in Schouveiler (1998).

We also note the results of the stability analysis of the Ekman–Couette flow with two Ekman boundary layers by Hoffmann, Busse & Chen (1998). In this configuration two parallel plates move relative to each other with a constant velocity in a system that rotates with an angular velocity normal to the plates. This study predicts a steady roll instability for a low rotation rate and instabilities of type I and type II for

increasing rotation rates. In a later study on the same Ekman–Couette flow Hoffman & Busse (2000) found an isolated solution describing a solitary vortex wave which does not seem to bifurcate from any other known solution. This solution is critical in a range of moderate rotation rates below the onset of type I instability, but is unstable with respect to three-dimensional disturbances.

Experimental studies on the stability of the Ekman layer by Faller (1963), Caldwell & Van Atta (1970) and others (see Crespo del Arco *et al.* 1996 for an extensive bibliography) have investigated the type I and type II instabilities. The three-dimensional rolls found in experiments have characteristic parameters (angle, phase velocity and wavelength) which are in reasonably good agreement with linear stability predictions. Savas (1987) studied experimentally unsteady uniformly rotating flow over a stationary disc and observed both type I and type II instabilities during the nonlinear phase of spin-down. Savas (1987) noticed the presence of both ring and spiral structures, the latter having angles between 12° and 18° for type I. In both the rotor/stator cavity and in the Ekman layer on a single disc, the experimental results exhibit similar spatial structures. However, the stationary disc and the confining geometry have an effect on the critical Reynolds number: $Re_{\delta c}$ is noticeably increased with respect to the standard Ekman configuration. Indeed Itoh (1991) made the estimates $Re_{\delta cII} = 85.3$ and $Re_{\delta cI} = 281$ for his experiment. Also, the experimental work of Sirivat (1991) studied the effect of geometry and rotation rate, concluding that the three modes of instability originate from different basic velocity fields.

The convective nature of spirals in the Ekman layer has been experimentally demonstrated (Lingwood 1996) by studying the response of the flow over a single rotating disc (von Kàrmàn boundary layer) to a local perturbation. In addition, the convective/absolute nature of the transitions in the boundary layer flow over a rotating disc has been demonstrated in both theoretical (Lingwood 1995) and experimental studies (Lingwood 1996). For the rotating flow over an infinite stationary disc, Lingwood (1997) also found theoretically the existence of this convective/absolute transition. The recent experimental results of Gauthier, Gondret & Rabaud (1999) of the instability of the flow between a stationary and a rotating disc have also revealed that the flow exhibits a convective/absolute transition in a rotor–stator cavity.

The evolution of the aforementioned types of flow and higher bifurcations have received relatively less attention in the literature. The experimental study of Schouveiler (1998), Schouveiler *et al.* (1999) presents the evolution and further transitions of the flow regimes for a wide range of values of the geometrical and control parameters. They report a variety of instability patterns depending on the aspect ratio of the cavity. For a basic state of Batchelor flow type, the critical instability has the form of annular rolls and spiral waves develop with positive angles for increasing rotation rate. When the basic state is a viscous flow – that is when the two boundary layers merge at high rotation rate – the critical instability consists of spiral rolls with negative angles, and also structures without spatial or temporal periodicity (such as solitary waves or spots) were observed far from the axis during the transition to turbulence (see also San'kov & Smirnov 1985). The stability analysis in the Ekman–Couette configuration of Hoffmann *et al.* (1998) also predicts secondary and tertiary transitions of the three types of flow (steady, type I and type II primary instabilities). Hoffman & Busse (2000) report that the solitary wave solution may correspond to the rollers observed in experiments on rotating discs but seems to have different nature and form from the solitary waves found by Cherhabili & Ehrenstein (1995) in the problem of plane Couette flow. The behaviour of non-modal perturbations in an Ekman layer flow has been investigated by Foster (1997), and the results explain

certain patterns noted in the atmospheric boundary layer by predicting other possible scenarios in the transition to turbulence. A wide range of nonlinear phenomena and instabilities in rotating flows has also been reported by Hopfinger & Linden (1990).

Recently, a number of direct numerical simulations of instabilities of boundary layers in rotating flow systems have been carried out. The evolution of type II waves in an Ekman layer was studied using a two-dimensional numerical method by Marlatt & Biringen (1995), but the two-dimensional computational results did not include the important effect of curvature nonlinear terms which give the possibility of obtaining circular and spiral roll waves. The circular waves observed in experiments have been obtained numerically in a rotor–stator cavity by solving the time-dependent axisymmetric Navier–Stokes and continuity equations by Crespo del Arco *et al.* (1996), Lopez & Weidman (1996), and Cousin-Rittemard (1996). However, these results were not fully satisfactory because they only considered axisymmetric models while, in general, the phenomena are three-dimensional. In recent works, Hugues *et al.* (1998) and Serre *et al.* (2001) obtained the first numerical simulation of spiral waves in a rotating cavity with a radial outflow by solving the three-dimensional governing equations.

In the present investigation we study the spatial structure and time dependence of flows which develop between a stationary and a rotating disc. Our direct numerical simulations exhibit some effects of curvature and geometrical confinement as previously noted in Serre, Crespo del Arco & Bontoux (1999). Two geometries are chosen in order to minimize the number of degrees of freedom in the numerical code, thereby reducing the computational time. The effect of weak curvature far from the rotation axis is studied with an annular geometrical configuration: the shaft–shroud model. This configuration reduces the radial domain and hence the required mesh resolution. The two geometric parameters used to define a cavity are the aspect ratio $L = \Delta R/2h$ and the curvature parameter $R_m = (R_1+R_0)/\Delta R$. A moderate cavity aspect ratio $L = 5$ is considered with curvature parameters $R_m = 4$ and 5. To investigate large curvature effects, a cylindrical cavity involving the axis is also considered and here aspect ratios $L = 2$ and 5 are relevant to a wide range of experimental configurations (Sirivat 1991; Schouveiler *et al.* 1999; Savas 1987; Gauthier *et al.* 1999). A pseudospectral Chebyshev–Fourier method associated with a multi-step time scheme is used. The spectral methods are particularly efficient in terms of accuracy with respect to the number of polynomials. Moreover, the use of the Chebyshev collocation approximation is readily adapted to concentrating grid points in the thin layers bordering the domain. The methods also guarantee a small phase error for the time-dependent simulations (Gottlieb & Orszag 1977; Canuto *et al.* 1988). The results were carried out for various rotation rates and geometrical configurations and the solutions, axisymmetric and three-dimensional, exhibit instabilities in the form of circular rolls or spiral vortices. These structures show great similarities with those described in the literature.

The presentation will be given as follows. The geometrical models are described in § 2 and the mathematical model and numerical solution technique are delineated in § 3. The structure of the basic stable flow is given in § 4. The results presented in § 5 are analysed in detail and compared with other investigations, both experimental and theoretical. A discussion of results is given in § 6 and concluding remarks are made in § 7.

2. Geometrical model

The geometrical models correspond to two discs enclosing either a cylindrical or an annular domain of radial extent $\Delta R = R_1 - R_0$, where R_0 and R_1 are the internal

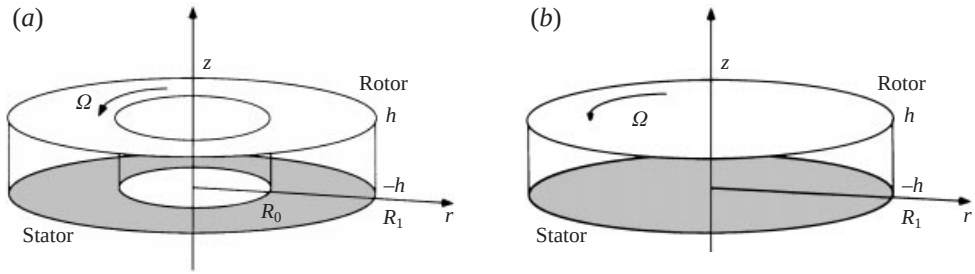

FIGURE 1. Schematic diagram of the rotating cavities. (*a*) Annular cavity. (*b*) Cylindrical cavity.

and external radii. The cavity that includes the axis, $R_0 = 0$, will be denoted the 'cylindrical' cavity while the case $R_0 \neq 0$ will be referred to as the 'annular' cavity. This last configuration is used to investigate curvature effects. These geometrical domains are bounded by one or two cylinders of height $2h$ as shown in figures 1(*a*) and 1(*b*); the origin of the z-axis is located at mid-height between the discs. The internal and external cylinders are denoted the shaft and the shroud, respectively. One disc of the cavity is stationary (stator) and the other (rotor) rotates at uniform angular velocity $\Omega = \Omega e_z, e_z$ being the unit vector on the axis. These configurations are basic cavity elements of a turbine engine.

3. Mathematical model and numerical method

3.1. *Physical parameters*

The flow is controlled by three major physical parameters: the relevant flow parameter is the Reynolds number Re and the two geometrical ones (which are also extremely important) are the aspect ratio of the cavity and the curvature parameter – defined in the following subsection.

The closed geometry is characterized by three independent length scales, R_0, R_1, h, each of which may be used in the definition of Re. In the literature the Reynolds number is based either on the external radius of the cavity, $Re_R = \Omega R_1^2/\nu$ (Owen & Rogers 1989; Schouveiler *et al.* 1999; Lopez & Weidman 1996), or on the height of the cavity, $Re = \Omega(2h)^2/\nu$ (Cousin-Rittemard 1996; Gauthier *et al.* 1999; Sirivat 1991). The latter is characteristic of the ratio between the thickness scale of the r-independent Ekman layer $\delta = (\nu/\Omega)^{1/2}$ (which also provides a good thickness scale of the Bödewadt layer) and $2h$, the height of the cavity. Then large values of Re are typical of the separated layers regime (Batchelor solution) while small Re are characteristic of the merged boundary layer regime (Greenspan 1972).

For sufficiently large values of Re, the boundary layers can be studied independently as a first approach as the flow over a single disc. As shown by analyses of the single infinite disc problem, the relevant Reynolds number is neither of the above, but rather the local Reynolds number $Re_\delta = \Omega\delta r/\nu$; note that this is the ratio between the local distance to the axis r and δ defined above. The Reynolds number Re_R then gives an upper bound to the square of the local Reynolds number Re_δ.

In the following, we will use Re as the general physical parameter but we will also incorporate Re_δ in the discussion of stability thresholds and characteristic wave parameters.

3.2. *Mathematical model*

The incompressible fluid motion is governed by the three-dimensional Navier–Stokes equations which are written below in primitive variables. The two geometrical parameters that appear are the curvature parameter $R_m = (R_1 + R_0)/\Delta R$ and the aspect ratio $L = \Delta R/2h$. For the 'cylindrical' cavity the only geometrical parameter is $L = R_1/2h$, since $R_m = 1$. The scales for the dimensionless variables of space, time and velocity are $[h, \Omega^{-1}, \Omega R_1]$ respectively. The dimensionless axial and radial coordinates are $z = z^*/h$, $z \in [-1, 1]$ and $\bar{r} = r^*/h$, $\bar{r} \in [L(R_m - 1), L(R_m + 1)]$, respectively. The radius $\bar{r}$ has been normalized on $[-1, 1]$, a requisite for the use of Chebyshev polynomials: the normalized variable is r with $r = (\bar{r}/L - R_m)$.

Along the cylindrical coordinate directions (r, θ, z) the velocity components are (u, v, w) respectively, and p is the pressure. Using the above space and time scales, the dimensionless continuity and momentum equations may be written in an absolute frame of reference:

$$\frac{1}{L}\frac{\partial u}{\partial r} + \frac{u}{L(R_m + r)} + \frac{1}{L(R_m + r)}\frac{\partial v}{\partial \theta} + \frac{\partial w}{\partial z} = 0,$$

$$\frac{\partial u}{\partial t} + L(R_m + 1)Au = -(R_m + 1)\frac{\partial p}{\partial r} + \frac{4}{Re}\left[\Delta u - \frac{u}{L^2(R_m + r)^2} - \frac{2}{L^2(R_m + r)^2}\frac{\partial v}{\partial \theta}\right],$$

$$\frac{\partial v}{\partial t} + L(R_m + 1)Av = -\frac{(R_m + 1)}{(R_m + r)}\frac{\partial p}{\partial \theta} + \frac{4}{Re}\left[\Delta v - \frac{v}{L^2(R_m + r)^2} + \frac{2}{L^2(R_m + r)^2}\frac{\partial u}{\partial \theta}\right],$$

$$\frac{\partial w}{\partial t} + L(R_m + 1)Aw = -L(R_m + 1)\frac{\partial p}{\partial z} + \frac{4}{Re}[\Delta w];$$

with the advection terms written as

$$Au = \frac{1}{L}u\frac{\partial u}{\partial r} + \frac{v}{L(R_m + r)}\frac{\partial u}{\partial \theta} + w\frac{\partial u}{\partial z} - \frac{v^2}{L(R_m + r)},$$

$$Av = \frac{1}{L}v\frac{\partial v}{\partial r} + \frac{v}{L(R_m + r)}\frac{\partial v}{\partial \theta} + w\frac{\partial v}{\partial z} + \frac{vu}{L(R_m + r)},$$

$$Aw = \frac{1}{L}u\frac{\partial w}{\partial r} + \frac{v}{L(R_m + r)}\frac{\partial w}{\partial \theta} + w\frac{\partial w}{\partial z}$$

where the cylindrical Laplacian operator is defined by

$$\Delta = \frac{1}{L^2}\frac{\partial^2}{\partial r^2} + \frac{1}{L^2(R_m + r)}\frac{\partial}{\partial r} + \frac{1}{L^2(R_m + r)^2}\frac{\partial^2}{\partial \theta^2} + \frac{\partial^2}{\partial z^2}.$$

No-slip boundary conditions apply at each impermeable wall. Thus $u = w = 0$ on all rigid walls. For the azimuthal velocity, the boundary conditions are $v = 0$ on the stator ($z = -1$) and $v = (R_m + r)/(R_m + 1)$ on the rotating disc ($z = 1$). The junction of the stationary cylinder with the rotor involves a singularity of the azimuthal velocity, as previously noted by Maubert *et al.* (1993). This singular condition expresses a physical situation where there is a thin gap between the edge of the rotating disc and the stationary sidewall, and we have retained this condition in the 'cylindrical' model since it is relevant to experimental devices. In the 'annular' model, the boundary conditions have been regularized with a virtual wall that produces a linear azimuthal velocity profile, as proposed by Cousin-Rittemard (1996) and Cousin-Rittemard, Daube & Le Quéré (1998). This linear profile is interesting from a mathematical point of view because it reduces sources of errors that could affect the numerical

solution. The two-dimensional results of these authors also provided benchmark solutions to our computations as they were the first to provide an explanation of the phenomenon of the direct transition from a steady to a time-dependent 'chaotic' boundary layer that was also observed in slender cavities by Maubert *et al.* (1993): the origin was attributed to curvature and confinement effects. For the range of parameters (L, Re) considered in this work, Serre (2000) has shown that similar patterns are nevertheless obtained with both the actual (discontinuous) and the academic (regularized) boundary conditions; the only slight differences (at the same Reynolds number) concern the near-shroud region but do not affect the layer of the stationary disc. At the shaft ($r = -1$) and at the shroud ($r = 1$) a continuous variation is considered in the form $v = (1+z)(R_m + r)/2(R_m + 1)$, $r = \pm 1$.

The initial condition corresponds to no motion in the meridional plane and to a linear shear profile for the azimuthal velocity:

$$u = w = 0, \qquad v = \frac{(R_m + r)}{2(R_m + 1)}(1 + z) \qquad \text{for} \qquad -1 \leqslant r, \;\; z \leqslant 1.$$

For the cylindrical cavity there is no physical boundary condition at the axis $R_0 = 0$. The dimensionless mathematical model is then slightly different and incorporates transformed dependent variables, as a requirement for numerical approximation. A natural zero condition is imposed on the axis by considering the new dependent variables $\tilde{\Psi} = \bar{r}\Psi$ with $\Psi = (u, v, w, p)$ as proposed by Serre & Pulicani (2001).

3.3. *Numerical method*

The numerical solution is based on a pseudospectral collocation Chebyshev–Fourier Galerkin method (see Canuto *et al.* 1988). The choice takes into account the orthogonality properties of Chebyshev polynomials and, in particular, provides exponential convergence – referred to as spectral accuracy (Gottlieb & Orszag 1977). Moreover the use of the Gauss–Lobatto collocation points, corresponding to the extrema of the Chebyshev polynomials of high degree, N and M in the radial and axial directions respectively, directly ensures high accuracy of the solution inside the very narrow wall layers.

The differential equations are exactly satisfied at the Gauss–Lobatto collocation points, $(r_i, z_j) \in [-1, 1] \times [-1, 1]$:

$$r_i = \cos\left(\frac{i\pi}{N}\right), \quad z_j = \cos\left(\frac{j\pi}{M}\right) \quad (i = 0, \ldots, N; \quad j = 0, \ldots, M).$$

The approximation of flow variables $\Psi = (u, v, w, p)$ and their derivatives is derived from the following truncated series:

$$\Psi_{NMK}(r, z, \theta, t) = \sum_{p=K/2}^{K/2-1} \sum_{n=0}^{N} \sum_{m=0}^{M} \hat{\Psi}_{nmp}(t)\, T_n(r)\, T_m(z)\, e^{ip\theta} \quad \text{for} \quad \left\{ \begin{array}{l} -1 \leqslant r, z \leqslant 1 \\ 0 \leqslant \theta \leqslant 2\pi \end{array} \right\},$$

$$\frac{\partial^q \Psi_{NMK}}{\partial r^q}(r_i, z_j, \theta_k, t) = \sum_{\eta=0}^{N} dr_{i\eta}^{(q)}\, \Psi_{NMK}(r_\eta, z_j, \theta_k, t),$$

$$\frac{\partial^q \Psi_{NMK}}{\partial z^q}(r_i, z_j, \theta_k, t) = \sum_{\xi=0}^{M} dz_{j\xi}^{(q)}\, \Psi_{NMK}(r_i, z_\xi, \theta_k, t),$$

where $dr_{ij}^{(q)}$and $dz_{ij}^{(q)}$ correspond to the coefficients of the matrix of first and second

derivatives ($q = 1, 2$) and where $\theta_k = 2\pi k/K$, $k = 0, \ldots, K-1$, are azimuthal points. An expansion of these coefficients based on the sinus function (Rothman 1991) is used to reduce the round-off error. T_n and T_m are Chebyshev polynomials and $\hat{\Psi}_{nmp}$ are the spectral coefficients defined by

$$\hat{\Psi}_{nmp}(t) = \frac{1}{K}\frac{1}{c'_n}\frac{1}{c'_m} \sum_{k=0}^{K-1} \sum_{i=0}^{N} \sum_{j=0}^{M} \frac{1}{c_i c'_j} \Psi(r_i, z_j, \theta_k, t)\, T_n(r_i)\, T_m(z_j)\, \mathrm{e}^{-\mathrm{i}p\theta_k}$$

with $c_0 = c_N = c'_0 = c'_M = 2$ and $c_n = c'_m = 1$ for $n = 1$, $N-1$ and $m = 1$, $M-1$. The unknowns are required to be real $\Psi(r_n, z_m, \theta_k)$ in physical space. The physical conditions are explicitly taken into account at the boundaries.

The time scheme is semi-implicit and second-order accurate. It corresponds to a combination of the second-order backward differentiation formula for the viscous diffusion term and the Adams–Bashforth scheme for the nonlinear terms; see Vanel, Peyret & Bontoux (1986). The velocity–pressure coupling is performed with a projection algorithm developed by Gresho & Sani (1987) for finite elements and applied by Raspo (1996) for three-dimensional spectral calculations. This algorithm has been modified by Hugues & Randriamampianina (1998) with an extension at each time step of a preliminary pressure, previously estimated at the initial step only. This procedure allows a possible temporal evolution of the normal pressure gradient at the boundaries. The modified algorithm is shown to reduce the slip velocity on the boundaries by one order of magnitude (compared to that of the temporal scheme) and it improves the incompressibility condition without the need of a shifted grid for the velocity and the pressure. At each time step the solution of the Navier–Stokes equations reduces to a solution of Helmholtz and Poisson type equations in Fourier space. A direct solver for these equations is used and based on a complete matrix diagonalization technique proposed by Haldenwang *et al.* (1984); for the annular cavity the matrices of radial and axial operators are diagonalizable with real eigenvalues and in the case of the cylindrical cavity the technique has been extended to complex eigenvalues. The numerical approximation method in this latter case was modified with the dependent variable transformation introduced above (§ 3.2) in order to take into account the central axis. Details of the technique are developed in Serre & Pulicani (2001).

3.4. *Spatial and temporal resolution*

The numerical strategy consists of increasing step by step the rotation rate from the base steady state to more complex flow regimes.

For the annular cavity, the accuracy of the solution was assessed by considering different grids and according to the value of the Reynolds number Re and of the curvature parameter R_m: the accuracy and the mesh dependence are reported in table 1 where some physical parameters of the solutions are compared. Some characteristic features of the three-dimensional flow structures are reported for $Re = 330$ and $Re = 400$; these are the instability frequency σ, the number of spiral arms, the number of rolls across the radial extent ΔR of the cavity, the deflection of the spiral angle ε from the direction of the geostrophic core flow, the normalized disturbance wavelength λ/δ, and the maximum of the axial velocity fluctuation. The physical meaning of the variables is discussed in § 5. It may be observed from table 1 that the solutions are almost identical with different meshes. The space and time scales of the instability differ by less than 0.1% and the major difference is observed in the magnitude of the perturbation $\tilde{w}$ (about 10%) that indicates the deflection from a

Mesh	σ	Number of spiral arms over 2π	Number of rolls in ΔR stator/rotor	ε (deg.) stator/rotor	λ/δ stator/rotor	$\lvert\tilde{w}_{\max}\rvert$ stator/rotor
(*a*) $48 \times 48 \times 48$	21.385	22	8	[11, 23]	[14.9, 20.45]	1.85×10^{-2}
			16	[−15.3, −6.9]	[9.4, 13.8]	5×10^{-3}
$64 \times 64 \times 48$	21.407	22	8	[11, 23]	[14.9, 20.43]	2.0×10^{-2}
			16	[−15.3, −6.9]	[9.4, 13.8]	5.5×10^{-3}
$152 \times 152 \times 48$	21.403	22	8	[11, 23]	[14.9, 20.40]	2.1×10^{-2}
			16	[−15.3, −6.9]	[9.4, 13.8]	5.7×10^{-3}
(*b*) $64 \times 64 \times 48$	16.790	18	10	[17, 30]	[13, 31.8]	7.0×10^{-3}
			14	[−20, −7.5]	[10, 15.2]	3.25×10^{-3}
$64 \times 64 \times 64$	16.801	18	10	[17, 30]	[13, 31.8]	7.1×10^{-3}
			14	[−20, −7.5]	[10, 15.2]	3.35×10^{-3}
$64 \times 64 \times 128$	16.801	18	10	[17, 30]	[13, 31.8]	7.05×10^{-3}
			14	[−20, −7.5]	[10, 15.2]	3.33×10^{-3}

TABLE 1. Mesh dependence of the solution: (*a*) in both (r, z) directions for a three-dimensional solution at $Re = 330$ in the annular cavity ($L = 5$, $R_m = 5$); (*b*) in the azimuthal direction for a three-dimensional solution at $Re = 400$ in the annular cavity ($L = 5$, $R_m = 4$). The upper and lower values of the parameters on ΔR are indicated in brackets.

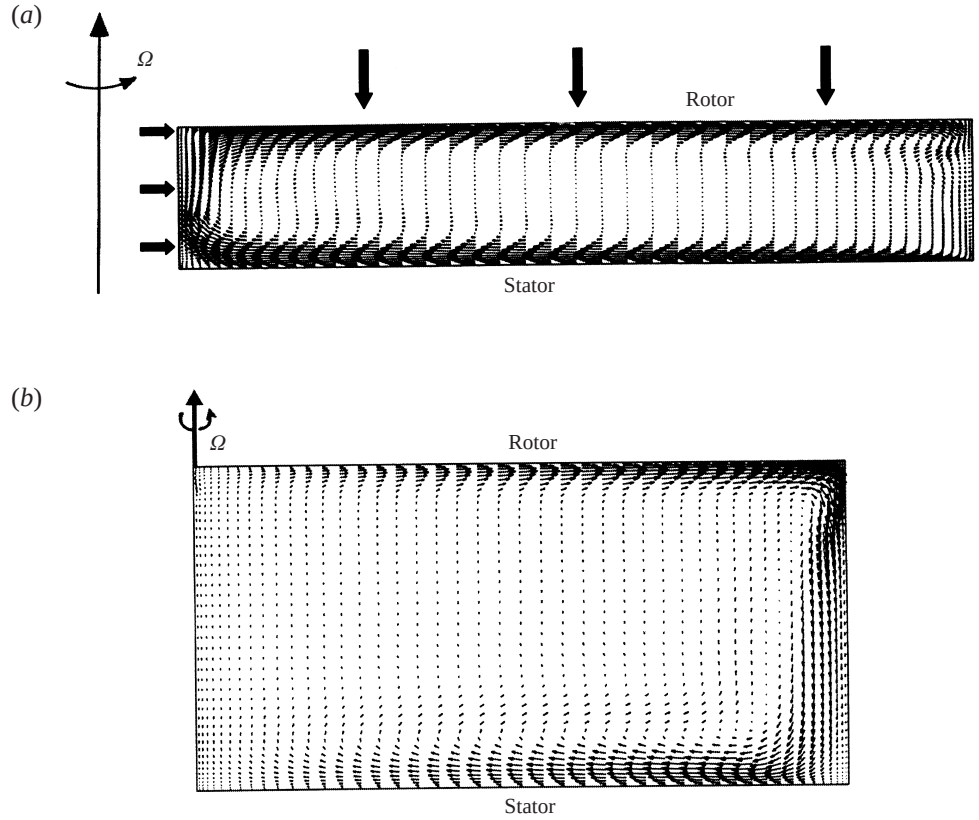

FIGURE 2. Basic flows of Batchelor type; velocity field in the plane $(r, z, \pi/4)$: (*a*) annular cavity ($R_m = 5$, $L = 5$) at $Re = 200$, (*b*) cylindrical cavity ($L = 2$) at $Re = 1400$. Black arrows outside the cavity (*a*) indicate the locations where the flow properties are stored for temporal analyses.

parallel flow. These tests and a former axisymmetric study of a rotating annular cavity (Crespo del Arco *et al.* 1996) indicate that spatial resolutions of 48×48 and 64×64 in (r, z), for $Re = 330$, $R_m = 5$ and for $Re = 400$, $R_m = 4$, respectively, constitute a good compromise between required accuracy and computational cost. The time steps incorporated are $\delta t = 4 \times 10^{-3}$ for $48 \times 48 \times 48$, $\delta t = 2 \times 10^{-3}$ for $64 \times 64 \times 64$ and $\delta t = 10^{-3}$ for $152 \times 152 \times 64$.

For the cylindrical cavity the grid refinement had to be increased due to nonlinear effects close to the axis: $64 \times 64 \times 48$, $123 \times 123 \times 48$ for $Re = 4000$, $L = 2$ and $123 \times 33 \times 48$ for $Re = 1600$ and $L = 5$. The time step incorporated is $\delta t = 10^{-3}$. Numerical details concerning the accuracy and solution dependence on mesh size are given in Serre & Pulicani (2001).

For the time-dependent solutions, the computing time is determined by the largest characteristic time in rotating flows, i.e. the viscous diffusion time $t_v = (2h)^2/v$ (Greenspan 1969); the dimensionless viscous time is equal to Re and the largest value is equal to 4000. Beyond one diffusion time, viscous effects have permeated the entire cavity and the small residual inertial oscillations are strongly damped.

Steady flow solutions are expected when the convergence rate becomes smaller than the relevant criterion $|U^{n+1} - U^n|/\delta t \leqslant 10^{-5}$ where U is the velocity vector, and the superscripts $n+1$ and n correspond to the time stages $(n+1)\delta t$ and $n\delta t$.

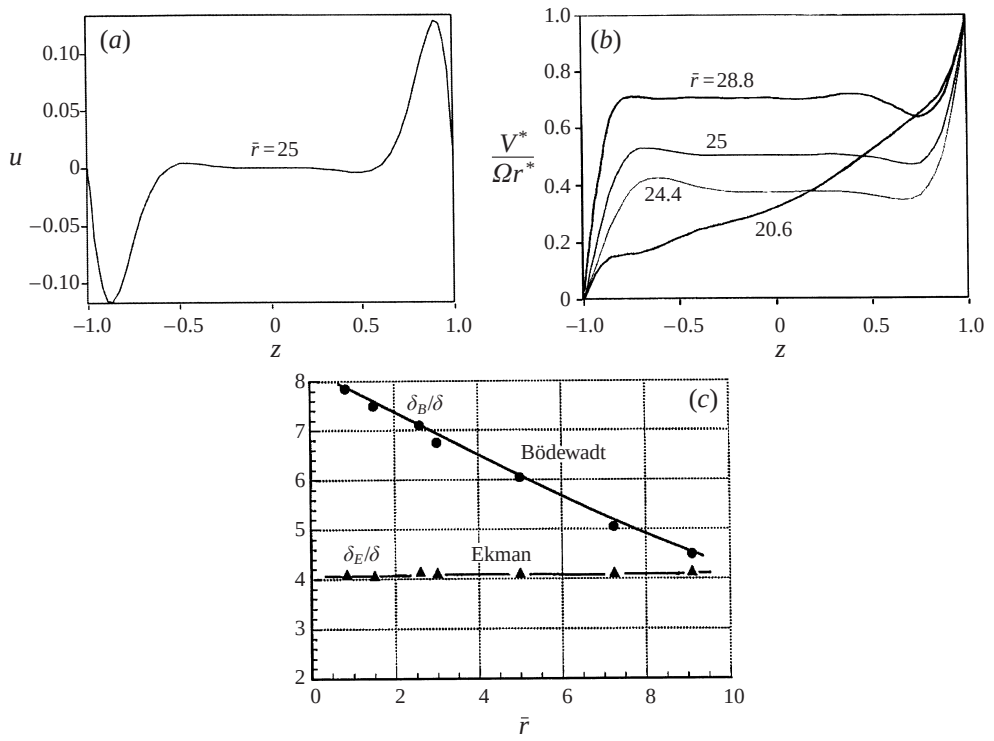

FIGURE 3. Axial profiles of the velocity in the annular cavity ($R_m = 5$, $L = 5$) at $Re = 200$: (*a*) radial component u at mid-radial location $r = 0$, (*b*) normalized azimuthal velocity at different radial locations. (*c*) Normalized thicknesses of both Ekman and Bödewadt layers, δ_E/δ and δ_B/δ with $\delta = (\nu/\Omega)^{1/2}$, measured at $Re = 1400$ in the cylindrical cavity ($L = 5$) and linear fit of the data.

4. Basic flow

The base flow solution is steady, axisymmetric, and composed of boundary layers on each disc and of a central core flow in near solid body rotation. These basic flow solutions have been displayed for the two configurations: in the annular cavity at $R_m = 5$, $L = 5$, $Re = 200$ (figure 2*a*) and in the cylindrical cavity $R_m = 1$, $L = 2$ for $Re = 1400$ (figure 2*b*). The z-profiles of radial and azimuthal velocity in the annular cavity $R_m = 5$ are given in figures 3(*a*) and 3(*b*) (at different radial locations), respectively. It is clear that the basic flow consists of two disjoint boundary layers above each disc which behave rather independently of each other, with fluid pumped radially outward along the rotating disc and radially inward over the stationary disc. These boundary layers are separated by the rigidly rotating core where the azimuthal component of velocity is independent of z (see Greenspan 1972). By analogy with the single disc problem, the boundary layer close to the rotating disc is called the Ekman layer (although Ekman layer solutions are linear, one retains this terminology in the nonlinear case) whereas the boundary layer close to the stationary disc is called the Bödewadt layer.

For infinite discs at sufficiently large rotation rates, similarity studies give a solid-body angular velocity $v^*(z = 0)/(\Omega r^*) = \beta$ where β is a constant, 0.313, as theoretically determined by Itoh (1991) for $Re = 1000$. This parameter is a Rossby number that measures the ratio between convective and Coriolis effects and which links the rotation speed of the disc (that we actually control) and the thickness scale of the

Bödewadt layer, $\delta_B = (\nu/\Omega_f)^{1/2}$, $\Omega_f r^* = v^*(z = 0)$. Unlike the similarity studies, we observed a radial variation of the parameter β and its value at the centre of the cavity is 0.53 (figure 3*b* for $\bar{r} = 25$), which is about 70% larger than the value predicted by the similarity studies. A comparison with available values of β in confined and non-confined geometries can be found in Randriamampianina *et al.* (1997) and an analytical expression for β as a function of radius is proposed in Owen & Rogers (1989) and Rott & Lewellen (1966). The radial evolution of β is emphasized in figure 3(*b*) which displays the normalized velocity profile $v^*/\Omega r^*$ at $Re = 200$ for different radial locations. The core fluid rotation rate increases from the shaft to the shroud as noted in former studies. These profiles emphasize also the increase of the core width characterized by $v^* = \beta\Omega r^*$. From the velocity field (figure 2*a*), we can see that this expansion of the core with the radius corresponds to a decrease of the Bödewadt layer thickness. Moreover, we show (figure 3*c*) the normalized (by δ) thicknesses of both Ekman and Bödewadt layers, in the case of the cylindrical cavity $L = 5$: for a given rotation rate, the Ekman layer remains constant in $\bar{r}$ whereas the Bödewadt layer thickness monotonically decreases from the shaft to the shroud, as experimentally noted by Gauthier *et al.* (1999). Our results closely fit the trend shown by these authors and nicely complete their measurements in the near-axis region where they are missing.

A comparison between the numerical results for finite configurations and the self-similar theoretical results for infinite discs shows that radial confinement can play a significant role; see Brady & Durlofsky (1986) for a discussion of finite disc effects. Nevertheless, the theoretical studies still provide qualitatively correct descriptions of our present solutions. Such behaviour of the base flow in confined geometries means that the radial flow is non-parallel and thus the description of the instability and the comparison with the literature require local scaling parameters. Although these numerical solutions do not completely satisfy self-similarity, they are still usually referred to as of Batchelor type.

5. Results

The investigation has been carried out for the two types of cavities shown in figure 1. For the annular cavity, the aspect ratio $L = 5$ and the curvature parameters $R_m = 4$ and $R_m = 5$ correspond to $\bar{r} \in [15;25]$ and $\bar{r} \in [20;30]$, respectively. We note that the $R_m = 5$ cavity is relevant to linear Ekman layers as shown in a preceding paper, Crespo del Arco *et al.* (1996). For the cylindrical cavity, the curvature parameter is $R_m = 1$ and the chosen aspect ratios are $L = 2$ for $\bar{r} \in [0;4]$ and $L = 5$ for $\bar{r} \in [0;10]$. The largest aspect ratio, $L = 5$, is a practical compromise between actual rotor/stator devices (that are of larger aspect ratio) and the computational cost of the numerical simulation. This cylindrical configuration is often used in fundamental experimental investigations. A wide range of behaviour has been reported for this type of cavity: the flows are stable in the near-axis region at small local Reynolds number Re_δ and unstable for $Re_\delta \geqslant Re_{\delta c}$. Annular and spiral structures arise at intermediate and great distances from the axis.

The velocity fluctuations, denoted by a tilde superscript in what follows, display the spatial structure of the instabilities. The time-dependent fluctuations are computed at given instants with respect to the average flow solution. When instability arises, the flow deviates from the parallel flow and then the perturbations are measured primarily by the magnitude of the axial component of velocity which varies about a zero mean.

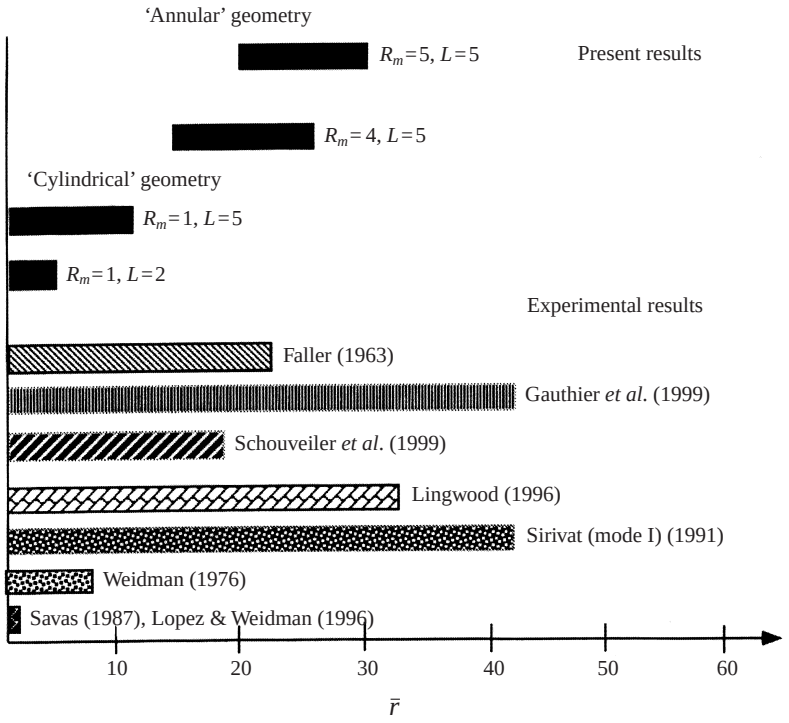

FIGURE 4. Sketch of various annular and cylindrical cavities in terms of radial extent $\bar{r}$: numerical model and actual devices from relevant experiments.

The dynamic behaviour of the dependent variables (u, v, w, p) is analysed at the nine significant (r, z, θ) points shown by the bold arrows in figure 2(*a*): three points $(-0.5, 0.95, \pi/4)$, $(0, 0.95, \pi/4)$, $(0.5, 0.95, \pi/4)$ close to the rotating disc, three points $(-0.5, -0.95, \pi/4)$, $(0, -0.95, \pi/4)$, $(0.5, -0.95, \pi/4)$ close to the stationary disc, and three points $(-0.5, 0, \pi/4)$, $(0, 0, \pi/4)$, $(0.5, 0, \pi/4)$ in the core.

The first goal of this section is to correlate numerical simulations and related experimental results reported by Savas (1987), Sirivat (1991), Lopez & Weidman (1996), Schouveiler *et al.* (1999), and Gauthier *et al.* (1999). Figure 4 shows the annular and cylindrical cavities in terms of radius variation together with the relevant experiments that are discussed in the following section. The instabilities appear as waves of circular or spiral form. They exhibit characteristics that are referred to as type I and type II instabilities of the Ekman and Bödewadt layers. The results have been obtained over computing times of the order of the viscous time and are summarized in table 2 for the annular cavity and in table 3 for the cylindrical cavity. Some relevant experimental and numerical results as well as results of the stability analysis are reported in tables 4 and 5 for the Bödewadt and the Ekman layers, respectively.

5.1. *Axisymmetric instability of the basic flow*

Two kinds of axisymmetric instabilities arise from the steady base flow (§4). One of them is stationary, presenting circular vortices, and the other is oscillatory and is characterized by travelling vortices in the Bödewadt and Ekman layers. The radial wavelength is defined as $\lambda_r = \Delta r^*/n_r$, where Δr^* is the radial length occupied by the n_r rolls. The wavelength is measured in terms of the Ekman layer length scale δ, as is usual in the literature.

	Rings stator/rotor			Spiral arms stator/rotor				
Re_R, Re, Re_δ	σ	λ_r/δ	$V^*_\Phi/\Omega r^*$	σ	λ/δ	$V^*_\Phi/\Omega r^*$	ε (deg.)	n
(*a*) 35000, 224, [112, 187]	*S*	—	—	—	—	—	—	—
45000, 288, [127, 212]	*S*	—	—	16.8	[13, 31.8]	[0.27, 0.40]	[17, 30]	18
					[15.2, 10]	[0.36, 0.13]	[−20, −7.5]	18
62500, 400, [150, 250]	4.76	[11, 17.6]	0.03	16.2; 8	[17.4, 20.5]	[0.30, 0.21]	[15.6, 23] and 0	18
		30	[0.08, 0.12]		[17.9, 11.4]	[0.30, 0.12]	[−20, −7.5]	18
(*b*) 35000, 156, [124, 187]	*S*	—	—	—	—	—	—	—
45000, 200, [141, 212]	*S*	—	—	16.3	[16.7, 11.6]	[0.30, 0.14]	[16, 24.1]	18
					[13.6, 25]	[0.25, 0.30]	[−19.7, −9]	18
75000, 330, [183, 274]	*O*	[6, 11]	0	21.4	[14.9, 20.4]	[0.28, 0.25]	[11, 23]	22
					[13.8, 9.4]	[0.26, 0.12]	[−15.3, −6.9]	22

TABLE 2. Characteristics of the numerical solutions in the annular cavities for different Reynolds numbers: (*a*) annular cavity ($L = 5$, $R_m = 4$), (*b*) annular cavity ($L = 5$, $R_m = 5$). The upper and lower values of the parameters along the radial direction are indicated in brackets. *S* denotes steady flow while $\sigma = 0$ denotes the stationary unstable solution.

	Rings stator/rotor			Spiral arms stator/rotor				
Re_R, Re, Re_δ	σ	λ_r/δ	$V^*_\Phi/\Omega r^*$	σ	λ/δ	$V^*_\Phi/\Omega r^*$	ε (deg.)	n
(*a*) 10000, 2500, [0, 100]	*S*	—	—	—	—	—	—	—
16000, 4000, [0, 127]	0.94	[10, 21]	[0.08, 0.02]	0.94; 2.82	[28.5, 16.1]	[0.68, 0.06]	0 and [25.5, 7]	6
(*b*) 20000, 800, [0, 141]	*S*	—	—	—	—	—	—	—
30000, 1200, [0, 173]	*S*	—	—	1	[45, 22.1]	[0.27, 0.02]	[28, 7]	6
40000, 1600, [0, 200]	4	[8, 25]	[0.13, 0.21]					

TABLE 3. Characteristics of the solutions in the cylindrical cavities for different Reynolds number: (*a*) cylindrical cavity ($L = 2$); (*b*) cylindrical cavity ($L = 5$). The upper and lower values of the parameters on ΔR are indicated in brackets.

References	Annular patterns								Spiral 3D patterns					
	L	H R (mm)	Re Re_R	$Re_{\delta c}$	λ/δ	σ	$V_\phi^*/\Omega r^*$	type	Re Re_R	$Re_\delta c$	λ/δ	σ	ε (deg.)	type
Measurements														
Gauthier *et al.* (1999)	20.9	6.7 140	110 48049	—	—	4	—	II	140 61153	—	—	—	$\varepsilon > 0$	I
Sirivat (1991)	21	12.07 254	88.6 39268	≈ 49	9.4	0	0.12	II	653 287973	400	38	—	—	I
	71.4	3 214	—	—	—	—	—	—	11.36 57912	140	6.74	—	—	I
Schouveiler *et al.* (1999)	8.75	16 140	225 17200	—	—	[3, 1]	[0.036, 0.05]	II	273 20900	—	—	2.1	25	I
Savas (1987)	2	214.8 107.4	38528 9632	35	[11, 25]	5	—	II	154124 38531	—	25	2.5	[12, 18]	I
Theory									—	15.1	16.6	—	−33.2	II
Faller (1991)	—	—	—	—	—	—	—	—	—	[15.1, 25]	—	—	—	I
Pikhtov & Smirnov (1993)	—	—	—	21	—	—	—	II	—	18.9	—	—	−22.4	II
2D simulations														
Lopez & Weidman (1996)	—	—	—	27.5	—	—	[0.083, 0.13]	II						
Cousin-Rittemard (1996)	[3, 10]	—	—	[164, 316]	—	—	—	II						

TABLE 4. Summary of results on Bödewadt layer instabilities. The upper and lower values of the parameters on ΔR are indicated in brackets.

References	L	H (mm) R (mm)	$Re_{\delta c}$	λ/δ	σ	ε (deg.)	$V_\phi^*/\Omega r^*$	Type
Measurements								
Caldwell & Van Atta (1970)	18	125 2250	56.7	—	[7.5, 11]	—	—	II
Faller (1963) and	—	—	$Re_{\delta c} \leqslant 70$	[22, 33]	—	[−20, 5]	—	II
Faller & Kaylor (1966)	—	—	125	[9.6, 12.7]	—	[10, 16.3]	—	I
Weidman (1976)	0.26	291.8 7.8	60	20.4	—	[−7, −1]	—	II
Theory								
Lilly (1966)	—	—	55	21	12	−20	—	II
	—	—	110	11.9	5	7.5	—	I
Faller & Kaylor (1966)	—	—	55	24	—	−15	—	II
	—	—	118	11	—	[10, 12]	—	I
Faller (1991)	—	—	54.3	20.1	—	−23.1	—	II
	—	—	113.1	11.5	—	6.9	—	I
2D numerical simulations								
Crespo del Arco *et al.* (1996)	5	—	[74, 112]	[26, 29]	6	0	0.28	II

TABLE 5. Summary of results on Ekman layer instabilities. The upper and lower values of the parameters on ΔR are indicated in brackets.

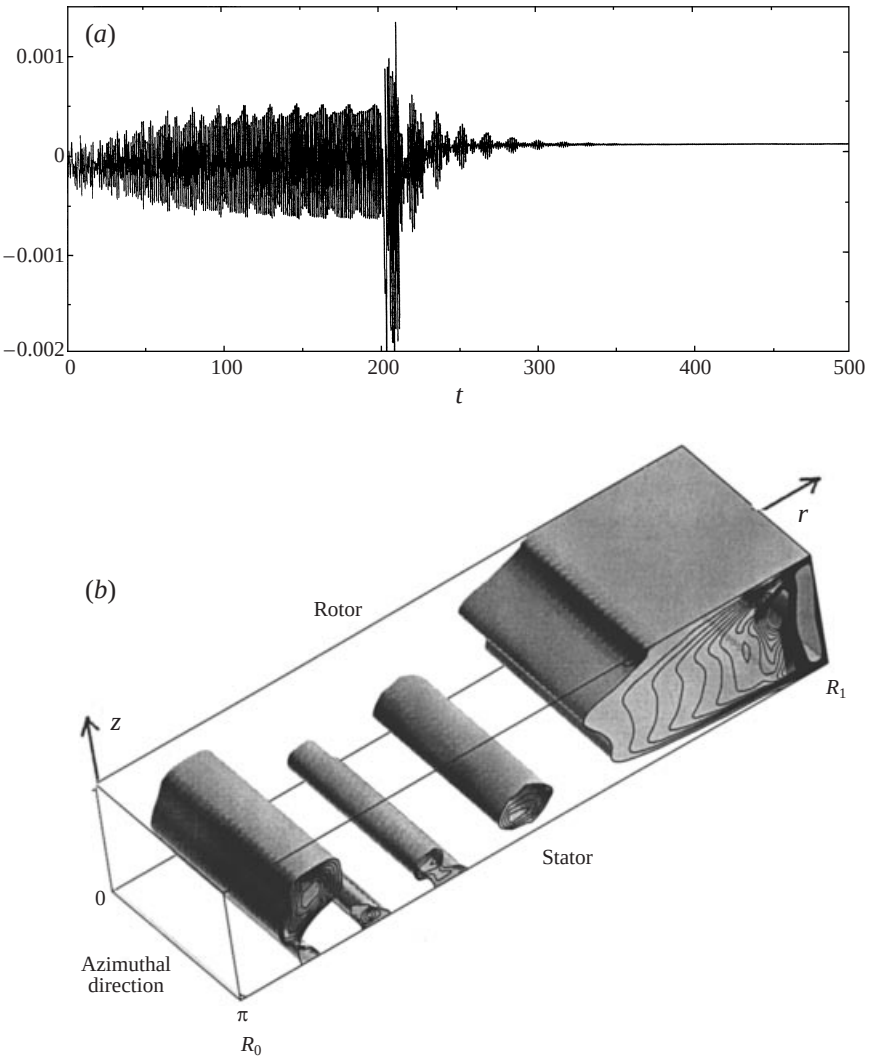

FIGURE 5. Stationary axisymmetric instability at $Re = 330$ in the annular cavity ($R_m = 5$, $L = 5$). (a) Time history of the solution close to the stationary disc $w\,(0, -0.95, \pi/4)$. (b) Three-dimensional display in a Cartesian frame of the axial velocity ($w = 3 \times 10^{-3}$) in the steady solution at $t = 450$.

5.1.1. *Stationary instability*

The basic Batchelor flow solution found at $Re = 200$ was described in § 4. For $Re = 330$, we found that the base flow is unstable to circular steady waves which appear on the stator wall. The stationary instability in the annular cavity ($R_m = 5$) is presented in figure 5(b). The time history is displayed in figure 5(a). The solution ultimately stabilizes over about one viscous time scale ($t_v = 330$ as may be seen in figure 5a) to yield three pairs of steady circular rolls near the stationary disc with variable wavelength $6 \leqslant \lambda_r/\delta \leqslant 11$, as seen in figure 5($b$). The stationary axisymmetric solution has features very similar to the experiments of Sirivat (1991) conducted for a cylindrical cavity of $L = 10.52$ at the smaller Reynolds number $Re = 88.6$. These experiments exhibited stationary circular rolls with a wavelength $9.4 \leqslant \lambda_r/\delta \leqslant 14$ that are related to the type II instability of the Bödewadt layer and appear quite similar to the present simulation.

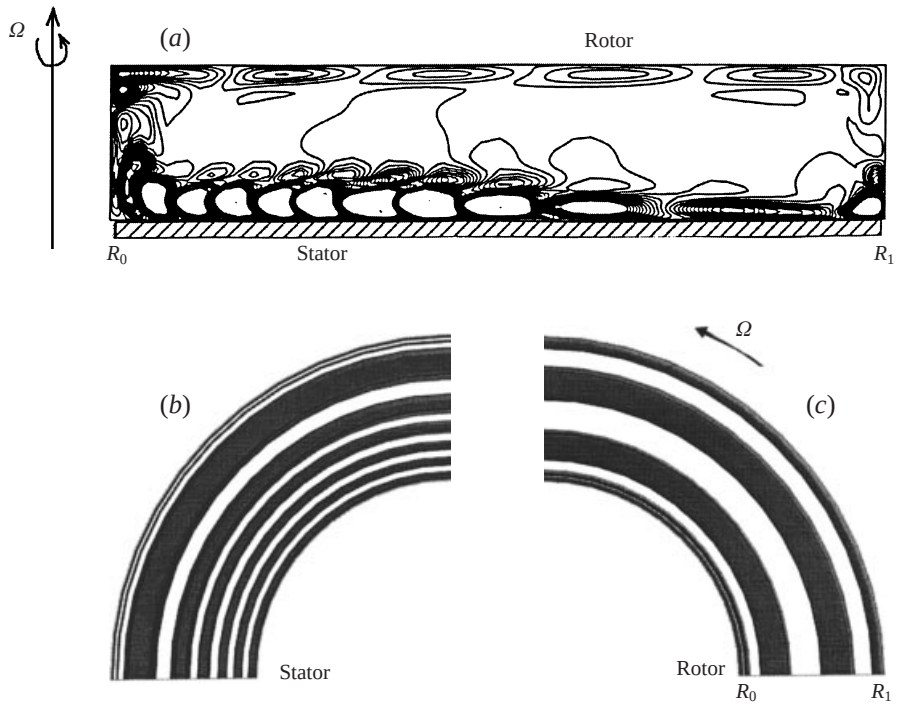

FIGURE 6. Time-dependent axisymmetric instability at $Re = 400$ in the annular cavity ($R_m = 4$, $L = 5$). (*a*) Iso-lines of the fluctuations of the axial velocity ($\tilde{w} = 3 \times 10^{-3}$) in the plane $(r, z, \pi/4)$. (*b*) Iso-surface of the fluctuations of the axial velocity ($\tilde{w} = 3 \times 10^{-3}$) close to the stationary disc in the plane $(r, -0.95, \theta)$ for $0 \leqslant \theta \leqslant \pi$. (*c*) Iso-surface of the fluctuations corresponding to the axial velocity ($\tilde{w} = 2 \times 10^{-4}$) close to the rotating disc in the plane $(r, 0.95, \theta)$ for $0 \leqslant \theta \leqslant \pi$.

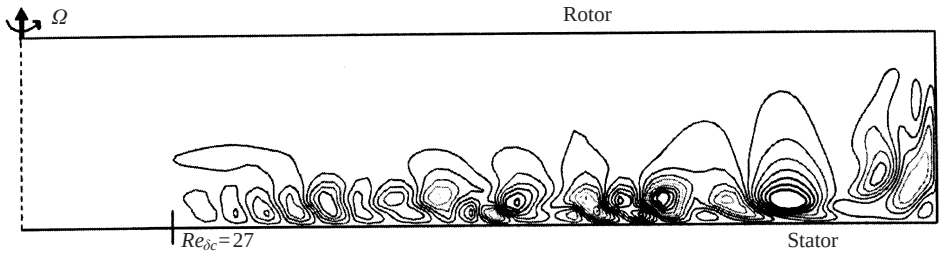

FIGURE 7. Time-dependent axisymmetric instability of the Bödewadt layer at $Re = 1600$ in the cylindrical cavity ($L = 5$) and in the plane $(r, z, \pi/4)$. Instantaneous iso-lines of the fluctuation of the axial velocity ($\tilde{w} = 4 \times 10^{-3}$). Critical local Reynolds number $Re_{\delta c} = 27$.

5.1.2. *Time-dependent instability*

When the rotation rate was increased, the instability became time dependent in both the annular ($L = 5$, $R_m = 4$) and the cylindrical ($L = 2$) cavities.

In the annular cavity, axisymmetric vortices are visible in the boundary layers of both the stationary and the rotating discs; see figure 6(*a*). In this figure (as in the following figure 9*b*) the iso-lines have been concentrated in the region of the lower value of the variable. This kind of display is chosen because it emphasizes the weaker disturbances close to the rotating disc but it exhibits the layer magnitudes with a

noticeable white surface inside the stronger disturbances close to the stator. The oscillatory solution ($\sigma = 4.7$) is reached after a transient of the order of the viscous time, namely $t = 300$ ($\simeq 2t_v/3$) for $Re = 400$. A lower frequency modulation $\sigma = 0.3$ is observed but vanishes after $t = 200$.

Inside the Ekman layer, three pairs of extended circular rolls with $19.5 \leqslant \lambda_r/\delta \leqslant 30$ propagate along the direction of the base flow and exhibit annular structures; see figure 6(*c*).

Inside the Bödewadt layer, about five pairs of counter-rotating rolls propagate radially inward (following the direction of the base flow), in the form of concentric rings; see figure 6(*b*). Outside the zones neighbouring the shaft and the shroud, the radial wavelength increases with radius and varies over the range of $11 \leqslant \lambda_r/\delta \leqslant 17.6$. The radial phase velocity $V_\phi = \lambda_r\sigma/(2\pi)$ decreases with radius over the range $0.08 \leqslant V_\phi^*/\Omega r^* \leqslant 0.12$.

Experiments by Gauthier *et al.* (1999) show the same kind of oscillatory axisymmetric patterns in a cylindrical cavity, but they appear far from the axis. Typical angular frequency and wavelength for their experiment are $\sigma = 4$ and $\lambda_r/\delta = 25.4$ at $Re = 128$ for a cavity of large aspect ratio, $L = 10.45$. The circular vortices propagate radially with diminishing phase velocity as $r \to 0$. An axisymmetric time-dependent instability has also been reported by Schouveiler *et al.* (1999) inside a Batchelor flow at $Re = 222$ for $L = 8.74$: there five pairs of circular rolls (that they named RC) appear close to the outer cylindrical wall and travel inward. Our results are also relevant to the numerical solutions of Cousin-Rittemard (1996) for an annular rotor/stator configuration and of Crespo del Arco *et al.* (1996) in the Ekman layers of an annular cavity subjected to a forced radial outflow. For $Re \simeq 800$, $R_m = 5$, Crespo del Arco *et al.* (1996) obtained rolls moving outward with $\sigma = 7.4$ and $\lambda_r/\delta \simeq 27$, qualitatively similar to our present results close to the rotor. For the same parameter values Cousin-Rittemard (1996) achieved the same spatial and temporal behaviour in the two layers with $\sigma = 4.7$ and $\lambda_r/\delta \simeq 27$ close to the rotating disc and $\lambda_r/\delta \simeq 15$ close to the stationary disc.

In cylindrical cavities (closer to the axis, $\bar{r} \leqslant 10$), the axisymmetric instability appears for $Re = 4000$, $L = 2$ and $Re = 1600$, $L = 5$. In contrast to the annular cavity, the vortices are present on the stator disc only – the Ekman layer on the rotating disc remains stable (figure 7).

For $L = 2$ at $Re = 4000$ a Hopf bifurcation is observed and the angular frequency $\sigma = 0.9$ is very close to the rotation frequency ($\sigma = 1$). This solution is characterized by four to five pairs of circular vortices with a radial wavelength $10 \leqslant \lambda_r/\delta \leqslant 21$ increasing with the radius. These vortices are observed over the external wall (stationary in this configuration) and travel inward along the Bödewadt layer to $\bar{r} = 0.5$ where they disappear; this final radius corresponds to a local Reynolds number $Re_\delta = 21$. The phase velocity of the circular waves is rather slow, varying over the range $0.02 \leqslant V_\phi^*/\Omega r^* \leqslant 0.08$. For the larger aspect ratio $L = 5$, the solution is time-dependent with a primary frequency $\sigma \simeq 4$. In this case we did not observe a transition to time-dependent flow via a Hopf bifurcation as for $L = 2$. The solution is characterized by vortices of radial wavelength $8 \leqslant \lambda_r/\delta \leqslant 25$ that vanish at $Re_\delta = 27$ (figure 7).

In the near-axis region (corresponding to the cavity $L = 2$) the present results are similar to the experimental findings of Savas (1987) for a cavity of aspect ratio $L = 0.5$. Savas (1987) was the first to observe travelling circular waves during impulsive spin-down of a fluid-filled cylinder for $25 \leqslant Re_f \leqslant 125$ where $Re_{fc} = 25$ is a critical Reynolds number based on the azimuthal component of the local velocity

vector in the core, $v^*(z = 0) = \Omega_f r^*$ where Ω_f is the angular velocity of the flow at the core and the subindex c stands for the critical value. Therefore, in order to compare with our Reynolds number $Re_{\delta c}$ (based on the local velocity of the disc) we have to multiply Re_{fc} by $\beta^{-1/2}$. As β varies with the radius (see § 4) we consider an average value, $\beta = 0.5$, from $L = 2$ and $L = 5$ computations in order to compare with our results. From our definition of local Reynolds number, the value given by Savas (1987) is $Re_{\delta c} \approx 35$, which is close to the one exhibited in our simulations, $Re_{\delta c} = 21$ for $L = 2$ and $Re_{\delta c} = 27$ for $L = 5$. Savas (1987) observed about nine pairs of rolls with a radial wavelength increasing with radius in the range of $10.5 \leqslant \lambda_r/\delta \leqslant 31$ and moving inward with an estimated phase velocity from his flow visualization of about $V_\phi = 0.135$ with a slight attenuation towards the centre to $V_\phi = 0.093$. The frequency $\sigma = 5$ reported by Savas (1987) is close to $\sigma = 4.76$ computed farther from the axis in the annular cavity ($R_m = 4$, $L = 5$) but it is however five times larger than $\sigma \simeq 1$ computed in the near-axis region (in the cylindrical cavity, $L = 2$). Schouveiler *et al.* (1999) also showed axisymmetric structures which travel inward with an angular frequency decreasing from $\sigma = 3$ (in a region close to the external wall) down to $\sigma = 1$ near the axis, in a zone very similar to the computational domain in the cylindrical cavity (see the sketch in figure 4); this behaviour is attributed to pairing phenomena (see § 6.1). Our results are also in good agreement with numerical results obtained with an axisymmetric model. In this near-axis region, numerical results by Cousin-Rittemard *et al.* (1998) also displayed a periodic solution, $\sigma = 0.88$, with five pairs of rolls over the stationary disc in a cylindrical cavity of aspect ratio $L = 2$. Moreover, the impulsive spin-down problem has been reconsidered both numerically and experimentally by Lopez & Weidman (1996) at $Re = 38528$ with $L = 0.5$. They report good agreement with Savas' results; in particular, they find inward propagating circular waves with a wavelength $9.8 \leqslant \lambda_r/\delta \leqslant 20$ and a phase velocity $V_\phi = 0.145$. A single pairing of the circular waves documented experimentally was found to be in excellent agreement with numerical simulation of the flow.

Thus, the present computed values of wave features ($\lambda_r, \sigma, V_\phi$) are in good agreement with previous experimental and numerical results. Following the analysis of Savas (1987), we conclude that the instabilities are of type II in both the Bödewadt and the Ekman layers.

5.1.3. *Circulation of the rolls in the annular cavity*

The vortices that arise in the stator layer are carried along the stator inward to the shaft where they are transported up to the rotating disc (figure 6*a*). We have observed that the rolls that travel all around the annular cavity do not correspond to a simple recirculation of disturbance structures. The structures grow in the Bödewadt layer and decay in the Ekman layer on the rotating disc (table 6). In the annular cavity ($R_m = 4$, $L = 5$), the magnitude of fluctuation is a maximum at the mid-stator location ($\bar{r} = 18$), where the base flow velocity is the largest (Serre 2000). The magnitude of the axial velocity fluctuation is then close to 2×10^{-2} which is about 50 times larger than the magnitude of the corresponding fluctuations near the rotating disc. In this process the vortices amplify in the stator layer from the shroud to $\bar{r} = 18$ and then diminish gradually while travelling further towards the shaft (the minimum of the axial velocity fluctuation gets close to 2×10^{-3}). Thus, the amplitude is abruptly damped on the shaft, at mid-height approximately, where the minimum is 5×10^{-4}. On the rotor the magnitude of the disturbance remains small with $\tilde{w} \approx 4 \times 10^{-4}$. Thus, we can consider that there is no feedback mechanism induced by the shaft and the shroud that enclose the cavity.

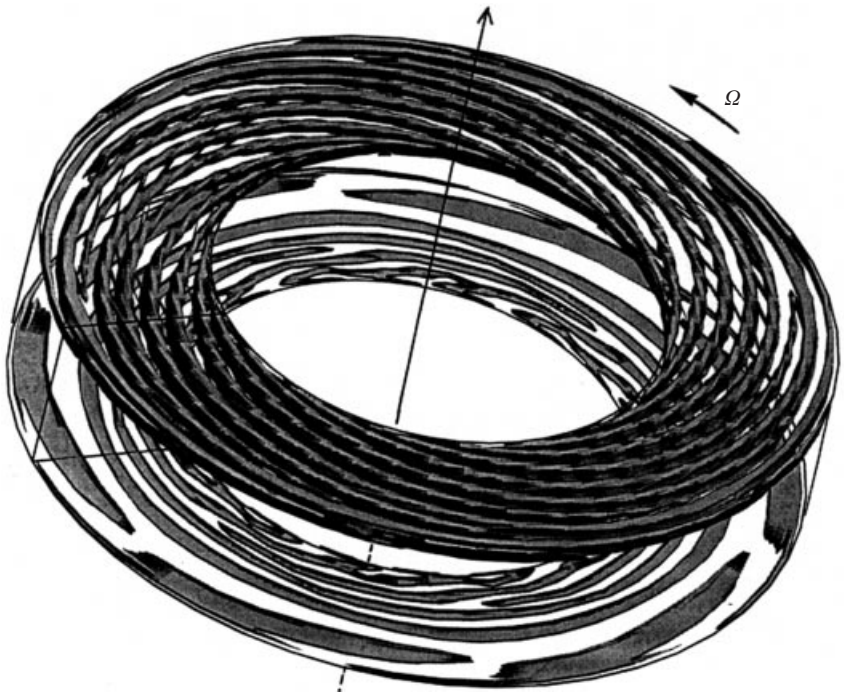

FIGURE 8. Complex spiral and annular patterns of the instability at $Re = 400$ in the annular cavity ($R_m = 4$, $L = 5$). Three-dimensional plot of the iso-surface of the fluctuation corresponding to the axial velocity ($\tilde{w} = 5 \times 10^{-4}$) in both Ekman and Bödewadt layers.

	$\bar{r} = 16$	$\bar{r} = 18$	$\bar{r} = 20$	$\bar{r} = 24.4$
$\lvert\tilde{w}\rvert \times 10^{-3}$ in $z = -0.8$ (stator)	2.25	20.02	5.05	3.52
$\lvert\tilde{w}\rvert \times 10^{-3}$ in $z = 0.8$ (rotor)	0.55	0.40	0.35	0.28

TABLE 6. Values of the axial velocity fluctuation at $Re = 400$ and at several radial positions $\bar{r}$ in the Ekman and the Bödewadt layers in the annular cavity ($L = 5$, $R_m = 4$).

5.2. *Three-dimensional instabilities*

The rolls that progress in the form of rings in the axisymmetric solutions now appear as spirals travelling within the cavity. One also observes the coexistence of ring and spiral patterns in the Bödewadt layer in annular and cylindrical geometries (figure 8). The three-dimensional flow was obtained by using as initial condition an axisymmetric solution and a three-dimensional perturbation superimposed on it. In experiments the onset of three-dimensional flows is spontaneous. Many reasons can be suggested, including: the convective/absolute nature of the instability, the necessity of finite-amplitude perturbations, and the restrictions imposed by a finite discretization. Many authors have argued in favour of the convective nature of the transition explaining this seeming mismatch between the experimental results and the present situation. In any case additional calculations would be needed at higher rotation rates and with a greater resolution in the azimuthal direction.

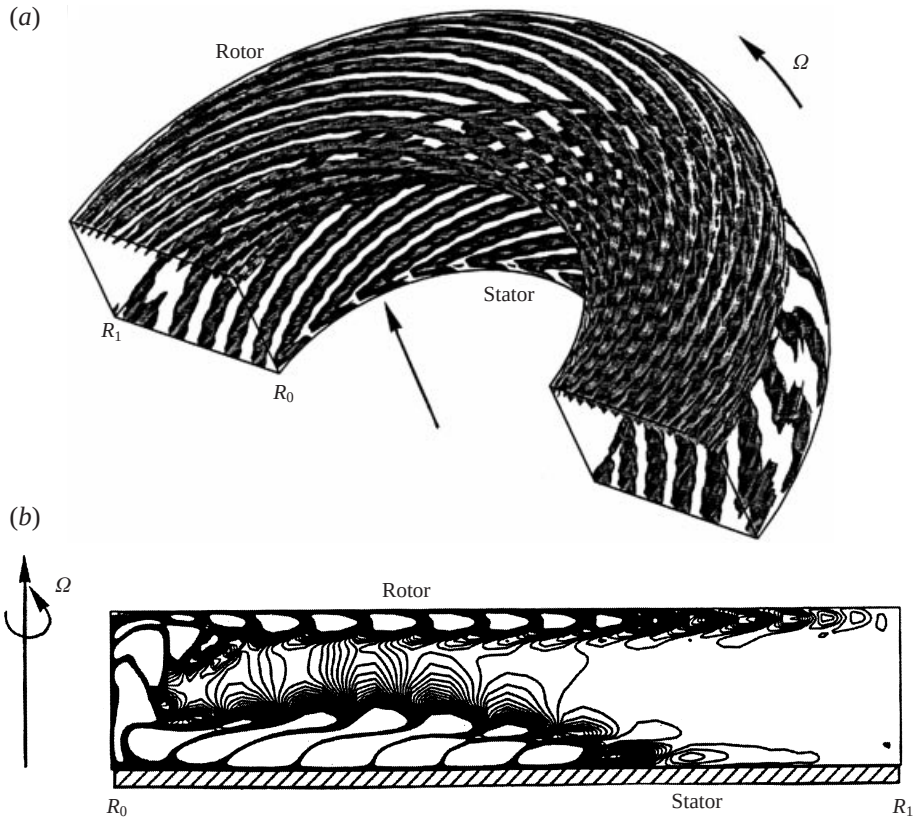

FIGURE 9. Spiral patterns of the instability at $Re = 330$ in the annular cavity ($R_m = 5$, $L = 5$). (*a*) Three-dimensional presentation of the iso-surface of the fluctuation of the axial velocity ($\tilde{w} = 8 \times 10^{-4}$) in both Ekman and Bödewadt layers. (*b*) Iso-lines of the fluctuation of the axial velocity ($\tilde{w} = 4 \times 10^{-4}$) in the plane $(r, z, \pi/4)$.

The general form of the disturbance is $\alpha \sin(p\theta)$ where p is an arbitrary number corresponding to an azimuthal wavelength and α is the amplitude rate. A typical value of α is 0.05 and we have obtained for each value of α a transition to three-dimensional flow. The effect of α on the transient has been investigated in the case of a rotating cavity subjected to a radial outflow (Serre *et al.* 2001); this reports an $\alpha^{-1/3}$ dependence of the transient time needed to reach the stabilized state. The disturbance is superimposed locally near the shroud at about $L(R_m + 0.7) \leqslant \bar{r} \leqslant L(R_m + 1)$. The same three-dimensional results are obtained irrespective of whether the azimuthal velocity or the other components of the velocity are perturbed and for three different disturbances of the azimuthal wavelength: $p = 2\pi/3$, $2\pi/8$ and $2\pi/12$. The exact divergence-free constraint is rapidly satisfied after a few preliminary iterations and a vortex structure grows or is damped depending on the initial flow conditions.

The orientation of the wave front is measured in terms of the angle ε with respect to the azimuthal direction of the geostrophic flow and which is defined positive when inclined towards the axis. The azimuthal wavelength is defined as $\lambda_\theta = 2\pi r^*/n$. The general wavelength of the spiral patterns can be defined by λ, as $\lambda = (2\pi r^*/n)|\sin(\varepsilon)| = \lambda_\theta |\sin(\varepsilon)|$, where n is the number of arms over 2π at the radius r^*.

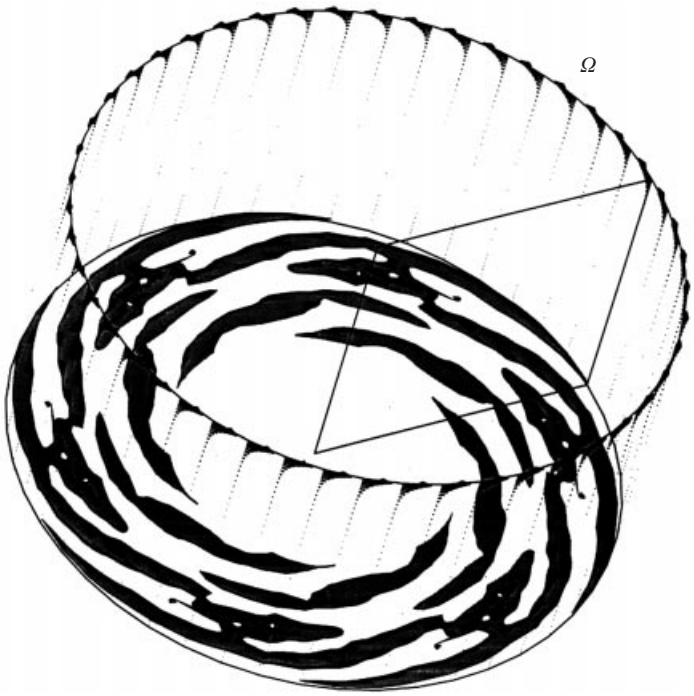

FIGURE 10. Three-dimensional instability of the Bödewadt layer at $Re = 4000$ in the cylindrical cavity ($L = 2$). View of the iso-surface corresponding to the fluctuation of the axial velocity ($\tilde{w} = 4 \times 10^{-3}$). Critical local Reynolds number $Re_{\delta c} = 33$.

5.2.1. *Pure spiral three-dimensional patterns*

Pure spiral patterns devoid of circular waves may be found in the ($L = 5, R_m = 5$) annular cavity far from the axis (figure 9*a*) and also in the near-axis region in the cylindrical cavity ($L = 2$) (figure 10).

In the annular cavity, the three-dimensional solution is obtained from the axisymmetric stationary flow given in § 5.1.1 for $Re = 330$. After a transient $t \simeq 250$ ($t_v = 330$), the solution is oscillatory ($\sigma = 21.4$) and a spiral structure with 22 arms arises in both layers.

Inside the Ekman layer, one can observe in figure 9(*b*) eight pairs of rolls in the radial direction, with a radial wavelength $12 \leqslant \lambda_r/\delta \leqslant 18$. The angle of the spiral wave front ε decreases with $\bar{r}$ over the range $-15.3^\circ \leqslant \varepsilon \leqslant -6.9^\circ$, the corresponding wavelength decreases with $\bar{r}$ over the range $9.4 \leqslant \lambda/\delta \leqslant 13.8$, and the phase velocity $V_\phi = \lambda\sigma/2\pi$ decreases with $\bar{r}$ over the range $0.12 \leqslant V_\phi^*/\Omega r^* \leqslant 0.26$. These three-dimensional spiral patterns have already been observed in experiments on the Ekman layer; see the review in Faller (1991). Caldwell & Van Atta (1970) and Faller & Kaylor (1966) found similar structures in experiments (spiral arms with a wavelength $22 \leqslant \lambda/\delta \leqslant 33$ and angles $-20^\circ \leqslant \varepsilon \leqslant 5^\circ$) that they referred to as a type II instability of the Ekman layer. The spiral structure of the computed rotor layer shows the same characteristics as the type II standard instability of the Ekman layer.

The spiral vortices on the stationary disc exhibit some similarity with those on the rotating disc but with positive angles $11^\circ \leqslant \varepsilon \leqslant 23^\circ$, which reveals a greater inclination with respect to the geostrophic flow. The wavelength of the spiral wave front near the stator is $14.9 \leqslant \lambda/\delta \leqslant 20.4$, slightly larger than on the rotating disc.

The spiral wave fronts propagate inward with a phase velocity which varies with the radius as $0.25 \leqslant V_\phi^*/\Omega r^* \leqslant 0.28$.

In the near-axis region $\bar{r} \leqslant 4$ (cylindrical cavity, $L = 2$), similar three-dimensional spirals develop after a short transient time of about $t = 20$ after the disturbance is superposed onto the axisymmetric flow for $Re = 4000$. The temporal behaviour exhibits a transition from an oscillatory axisymmetric solution ($\sigma = 0.9$) to a quasi-periodic-type flow with two major frequencies equal to $\sigma = 0.9$ and $\sigma = 2.8$. Here four to five pairs of rolls are observed on the stationary disc with a radial wavelength that remain close to $\lambda_r/\delta \simeq 25$. The rotating disc layer and the near-axis region remain unperturbed as in the axisymmetric solution, in agreement with the local Reynolds number criterion for the onset of the Ekman layer instability. The critical Reynolds number $Re_{\delta c}$ is roughly 33 on the stationary disc, very close to the experimental criterion determined by Savas (1987) $Re_{\delta c} \approx 35$ (see § 5.1.2). During the transient, axisymmetric patterns are observed in the intermediate radial region $1 \leqslant \bar{r} \leqslant 2$ corresponding to $33 \leqslant Re_\delta \leqslant 63.5$ while the axisymmetric rolls immediately transform into spiral structures farther from the axis. This behaviour is in accord with some cases to be considered in § 5.2.2. The axisymmetric structures then vanish and only six spiral arms are observed after stabilization (see figure 10). The angle ε with the geostrophic flow significantly decreases with $\bar{r}$, with values $\varepsilon = 25.7^\circ$ at $\bar{r} = 2$ and $\varepsilon = 7^\circ$ at $\bar{r} = 4$; the corresponding wavelengths vary over the range $16.1 \leqslant \lambda/\delta \leqslant 28.5$. These spiral patterns have already been observed in experiments in a Bödewadt layer by Schouveiler *et al.* (1999) at $Re = 257.4$, $L = 8.75$: the spiral patterns (denoted RS1) evolve close to the shroud with an angle of $\varepsilon = 25^\circ$ but are described as propagating outward, opposite to that obtained in our direct numerical simulation.

The computed values of λ, and particularly the positive values of ε for these spiral waves, are in good agreement with previous experimental and numerical results. Again following the analysis of Savas (1987) the instability of the Bödewadt layer is supposed to be of type I.

An iso-surface corresponding to the axial velocity fluctuation ($\tilde{w} = 5 \times 10^{-4}$) is plotted in figure 11 for the cylindrical cavity ($L = 2$). The pattern exhibits two major features. Away from the shroud, vortices from the unstable Bödewadt layer rise up to the vicinity of the rotating disc. This suggests some pumping effect from the rotor of small magnitude. Near the shroud (which is stationary in this cavity), spiral arms appear and extend to about 80% of the height of the cavity. This vertical protrusion shows a typical helicoidal trajectory (see a recent note by Buisine, Oble & Andrianarahinjaka 2000). The overall impression from this plot is that the three-dimensional flow pattern is very complex.

5.2.2. *Mixed annular and spiral patterns*

The cylindrical cavity of larger aspect ratio ($L = 5$) and the annular configuration ($R_m = 4$, $L = 5$) are now considered to explore the effects of reducing the radial confinement and increasing the mean curvature, respectively. The spatial structure is more complex than that described above in § 5.2.1. We observe the coexistence of circular and spiral patterns inside the Bödewadt layer as well as dislocation phenomena in both layers.

In the annular cavity ($\bar{r} \in [15; 25]$), the three-dimensional solution is aperiodic but with two dominant frequencies, $\sigma_1 = 16.2$ and $\sigma_2 = 8$, while the unperturbed axisymmetric oscillatory solution was periodic ($\sigma = 4.7$). These frequencies are successively dominant at various locations. The smaller frequency σ_2 is dominant near the stationary disc boundary layer while σ_1 is dominant close to the rotating disc.

FIGURE 11. Complex three-dimensional instability at $Re = 4000$ in the cylindrical cavity ($L = 2$). View of the fluctuations of the axial velocity ($\tilde{w} = 5 \times 10^{-4}$) expanding from the Bödewadt layer (below) up to the rotating top wall.

The σ_1 disturbance also dominates at the rotor–shroud corner while both σ_1 and σ_2 disturbances are of similar magnitude at the rotor–shaft and stator–shroud corners.

The instability spatial structure inside the Ekman layer is shown in figure 12(*b*). There are seven pairs of rolls in the radial direction (figure 12*a*) and 18 spiral arms can be counted over 2π. The magnitude of ε decreases dramatically between the inner and the outer radii, ranging from $-20°$ to $-7.5°$, and the associated wavelength increases over the range $11.4 \leqslant \lambda/\delta \leqslant 17.9$. The vortices evolve outward, with a phase velocity V_ϕ as $0.12 \leqslant V_\phi^*/\Omega r^* \leqslant 0.30$. In figure 12(*b*), coalescence of spiral vortices between the shaft at R_0 and the shroud at R_1 produces a zone of dislocations which reduces the number of spiral arms (further details about this phenomenon are given in § 6.1). These spiral patterns have characteristic parameters (λ, ε) very close to those described previously in § 5.2.1 for $L = 5$, $R_m = 5$ and correspond to a type II instability.

In the Bödewadt layer, circular and spiral instabilities coexist (figure 12*c*). Four pairs of spiral and circular rolls of average radial wavelength $\lambda_r = 19.2$ and two pairs close to the shroud with a larger wavelength $\lambda_r = 26$ may be observed. The latter develop into rings and the former develop into 18 spiral arms with angles varying over the range $15.6° \leqslant \varepsilon \leqslant 23°$ close to the shaft in the region $15 \leqslant \bar{r} \leqslant 18$. The persisting axisymmetric structures interact with the spiral arms at $\bar{r} = 18$ and travel inward with a radial phase velocity $0.19 \leqslant V_\phi^*/\Omega r^* \leqslant 0.27$.

The coexistence of these two types of waves was first described by Savas (1987). He reported patterns that simultaneously involve spiral waves with 23 arms of positive

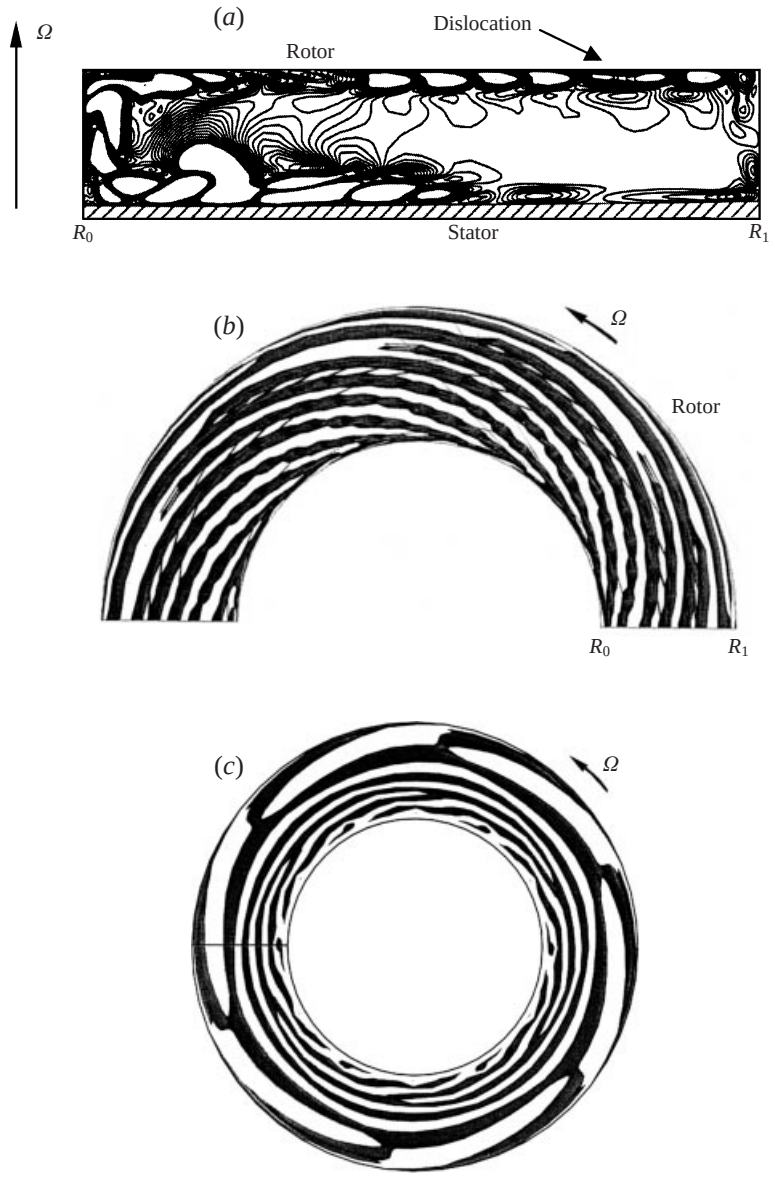

FIGURE 12. Pairing effects on the three-dimensional instability at $Re = 400$ in the annular cavity ($R_m = 4$, $L = 5$). (*a*) Iso-lines of the fluctuation of the axial velocity ($\tilde{w} = 3 \times 10^{-3}$) in the plane ($r$, z, $\pi/4$). (*b*) Iso-surface of the fluctuation of the axial velocity ($\tilde{w} = 3 \times 10^{-3}$) close to the rotating disc in the plane (r, 0.95, θ) for $0 \leqslant \theta \leqslant \pi$ and dislocation phenomenon. (*c*) Spiral and annular patterns of the Bödewadt layer: iso-surfaces of the fluctuation of the axial velocity ($\tilde{w} = 3 \times 10^{-3}$) close to the stationary disc in the plane ($r, -0.95, \theta$) for $0 \leqslant \theta \leqslant 2\pi$.

angle, ranging between 12° and 18°, towards the centre and circular waves. Savas (1987) identified these spirals as being a type I instability. The axisymmetric structures were exhibited close to the outer cylindrical wall as in our numerical solution.

In the cylindrical cavity ($\bar{r} \leqslant 10$, $L = 5$), the flow becomes unstable and vortices appear in the Bödewadt layer soon after a disturbance is superimposed on the steady axisymmetric solution obtained for $Re = 1400$. The temporal behaviour exhibits a

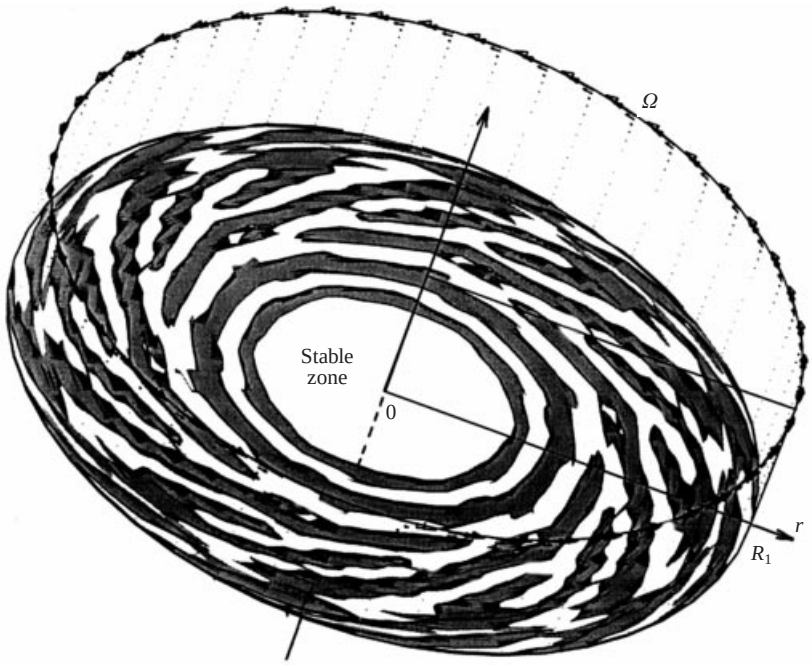

FIGURE 13. Spiral and annular patterns of the instability of the Bödewadt layer for $Re = 1200$ in the cylindrical cavity ($L = 5$). Three-dimensional view of the iso-surface corresponding to the fluctuation of the axial velocity ($\tilde{w} = 4 \times 10^{-3}$).

oscillatory regime with a dominant angular frequency nearly equal to the rotation frequency $\sigma \approx 1$ and very close to that computed for $Re = 4000$ and $L = 2$. Eight pairs of rolls of radial wavelength decreasing with radius over the range $8.8 \leqslant \lambda_r/\delta \leqslant 17$ move downstream to $\bar{r} = 1.54$, corresponding to $Re_\delta = 26.64$ with phase velocity $0.02 \leqslant V_\phi^*/\Omega r^* \leqslant 0.27$. For $1.54 \leqslant \bar{r} \leqslant 5$ for which $26.64 \leqslant Re_\delta \leqslant 86.5$, five circular waves evolve. At larger distance from the axis, spiral structures evolve with angles varying between $7° \leqslant \varepsilon \leqslant 28°$ (figure 13); the spiral arms exhibit dislocations that can be seen in figure 12(*b*). In contrast to the previous annular case ($R_m = 4$, $L = 5$) and experiments by Savas (1987), the spirals appear close to the outer wall at larger local Reynolds number Re_δ as in recent experiments by Schouveiler *et al.* (1999) and Gauthier *et al.* (1999) for $Re = 273$ and $L = 8.75$ and for $Re = 180$ and $L = 20.9$, respectively. Schouveiler *et al.* (1999) found about 16 spiral arms close to the shroud as in the cylindrical cavity for $Re = 1600$ and $L = 5$ and defined by an angle ε of about 25°. Thus it seems that these spiral structures correspond to the type I instability of the Bödewadt layer. Nevertheless, we cannot determine from the present results if the coexistence of these two types of structures is a consequence of the confinement effect or if it is provoked by different values of the local parameters.

6. Analysis and discussion

6.1. *Structural defects*

In extended systems (when the scale of the system is several times larger than the scale of the physical phenomenon), the constraint due to the geometry is weak: then, dislocations may appear and several patterns can be observed simultaneously.

The structural defects observed in our computations are related to variations in the wavelength of the structures. Indeed, it appears that various patterns (rings, spirals) are present in different flow regions so that structural defects are created at the junction between them. The coexistence of these different patterns and the dislocations at the junction are clearly evident in both layers of the annular cavity ($L = 5$, $R_m = 4$) in figures 12(*b*) and 12(*c*) at $Re = 400$ and close to the stationary disc in the cylindrical cavity ($L = 5$) at $Re = 1200$ (figure 13): dislocation phenomena arise either at the junction between circular and spiral waves (figures 12*c* and 13 in the Bödewadt layer) or between spiral arms of different azimuthal wavelengths (figures 13 and 12*b* in the Ekman layer). In all cases these structural defects are stationary. For example, in the Ekman layer of the annular cavity for $R_m = 4$, we observed six periodic dislocations over 2π at the fixed radial location $\bar{r} = 23.75$. In the azimuthal direction the phenomenon thus repeats every $\pi/3$ radians and consists of the coalescence of two successive spiral structures into one with a simultaneous disappearance of the third neighbouring vortex.

Structural defects have been reported for circular waves by Cousin-Rittemard (1996) at $700 \leqslant Re \leqslant 1000$, $L = 5$ and for a moderate distance from the axis, $R_m \simeq 2$, and later in experiments by Schouveiler *et al.* (1999) in the Bödewadt layer at $Re = 225$ in a cavity of aspect ratio $L = 8.74$. These authors have found axisymmetric waves travelling in the radial direction which have different wavelengths and different time frequencies in the two zones (small and large radii); at the junction the rolls undergo pairing. These authors reported that the pairing phenomenon of cylindrical waves is correlated to the local adjustment of phase velocity to the base-flow convective velocity. Indeed, since the radial wavelength (related to the thickness of boundary layer) does not vary very much over the radial domain, the frequency must vary: the phenomenon of dislocation is thus associated with a change in frequency. Structural defects at the junction between circular and spiral waves have been observed in experiments by Savas (1987) and more recently by Schouveiler (1998) and Gauthier *et al.* (1999). However to our knowledge the dislocation phenomenon when only spiral patterns are present has not been reported in experiments.

In our results, the spatial dislocation is not associated with a frequency change and the time behaviour is oscillatory with the same frequency in the whole boundary layer. However, the dislocations are related to the variation of the angle in the radial direction with respect to the azimuthal direction, the preferred angle that undergoes a discontinuous change while the phase velocity changes during dislocation. As mentioned above, this is a similar mechanism to the case of the circular patterns shown by Cousin-Rittemard (1996) and Schouveiler *et al.* (1999) but we did not observe vortex pairing of circular waves.

We should also mention the numerical studies of Lopez (1996) and Lopez & Weidman (1996) for circular waves. There, it is possible that the dislocation phenomenon would be a transient, but as we did not pursue the computation over several viscous times, we cannot assess whether our solution is completely established: the system would be able to evolve towards a solution similar to that in the annular cavity at $R_m = 5$ (figure 9).

6.2. *Thresholds of the succeeding regimes and hysteresis cycle*

We now describe a hysteresis cycle found in our numerical calculations in annular cavities on decreasing the rotation rate below the value where a spiral instability exists. The threshold was determined by superposing a three-dimensional perturbation of the axisymmetric solution while progressively decreasing Re from the spiral solution.

The three-dimensional spiral instability solution remained stable below the threshold of the Hopf bifurcation from the axisymmetric solution.

In the annular cavity ($R_m = 4$, $L = 5$) the critical value of Re below which the three-dimensional spiral instability disappears is $Re_c = 288$, while the Hopf bifurcation occurs at $Re = 400$. We note also that in the annular cavity for $R_m = 5$, the three-dimensional instability is again maintained down to $Re = 200$ while the steady instability of the axisymmetric solution occurs at $Re_c = 330$ followed by the oscillatory instability at $Re_c = 350$. We note for the two cases at different curvatures that the flow features vary differently: for $R_m = 4$ the spiral pattern is conserved with 18 arms on varying the rotation rate, while for $R_m = 5$ it evolves from 22 to 18. As a result, the frequency varies from 21.4 to 16.3 which is quite similar to the basic frequency level of about 16.8 observed at $R_m = 4$.

This hysteresis cycle could suggest a subcritical nature of the transition and complementary computations on the phenomenon are in progress.

6.3. *Some effects of curvature and confinement on flow behaviour*

The study of cavities with different values of R_m permits an investigation of phenomena associated with curvature effects. The circular and the spiral structures both exist at small and large distances from the axis (large and small curvature, respectively), but more complex spatial and temporal behaviours of the flow are observed as the curvature increases, as revealed for example by the dislocation phenomenon in both wall layers (see § 6.1).

Indeed, when the curvature effects are important ($L = 5$, $R_m = 1$) and ($L = 5$, $R_m = 4$), the three-dimensional spatial structure of the instability near the stationary disc exhibits the coexistence of circular and spiral patterns as observed by Savas (1987) and by Schouveiler *et al.* (1999), while only spiral arms are observed at larger distances from the axis ($L = 5$, $R_m = 5$) in both the Ekman and the Bödewadt layers.

The effect of the curvature on the temporal behaviour results in an increase of the nonlinearity of the problem (for $R_m \to 1$) and so the dynamical behaviour evolves rapidly to more complex regimes. Thus at large distances from the axis, the sequence of solutions corresponding to successive bifurcations can be easily observed. For instance in the annular cavity for $R_m = 5$, there is an exchange of stability from one steady flow without rings to another steady regime with rings, and when an azimuthal disturbance is superimposed onto the axisymmetric solution, it develops into an oscillatory spiral solution. Slightly nearer the axis, in the $R_m = 4$ cavity, the first transition observed is from a steady to an oscillatory solution and the three-dimensional disturbance produces a non-periodic regime. Further details about this aspect will be given in Daube *et al.* (2001). These authors investigated the linear and nonlinear stability of axisymmetric rotor–stator disc flows and they found in particular that for large radii the Hopf bifurcation is supercritical whereas at small radii this bifurcation seems to become subcritical.

The effect of confinement is to slow down the evolution to complex regimes, unlike the effect of curvature. For example in the near-axis region and the confined cavity ($R_m = 1$) of aspect ratio $L = 2$, a spatial structure with only spiral arms was observed and a Hopf bifurcation was obtained as in Cousin-Rittemard (1996).

6.4. *An equation for the spiral wave fronts*

We represent the rotating waves obtained in both Ekman and Bödewadt layers by a wave front equation based on a kinematic observation as

$$\bar{r} = f(\theta).$$

In a previous work, we have proposed an equation for the spiral wave front in the case of an Ekman layer arising in a rotating cavity subjected to a radial forced flow. It was observed that this wave front was not linear and followed a law $r^2 \propto \theta$ (for more details see Serre *et al.* 2001). More precisely, the location of the spiral wave front was given by

$$\bar{r}^2 = \frac{nLR_m}{3\pi}\left(\theta + \frac{2\pi \mathrm{i}}{n}\right),$$

and thus the angle made by the spiral arms with the geostrophic velocity varied as $\bar{r}^{-2}$ according to

$$\tan\psi = -\frac{nLR_m}{6\pi\bar{r}^2},$$

where n is the number of spiral arms over 2π. This equation still fits very well with our computations of the spiral arms arising close to the rotating disc in the annular cavities (figures 8, 9, 12*b*) which correspond to geometrical parameters (R_m, L) close to those of our previous study (Serre *et al.* 2001).

For the spiral wave fronts arising in the Bödewadt layer we have not determined a special equation (as in the case of the Ekman layer) but only a trend. For this purpose, we have measured the locations of several discrete points on the spiral arms. We have plotted (figure 14), in the $(\bar{r}, \theta)$-plane, the cylindrical coordinates of two consecutive arms of the computed spirals together with the data from the experiments by Schouveiler *et al.* (1999). Unlike the Ekman layer instability, the radius is seen to depend nearly linearly on the polar angle θ which is characteristic of an Archimedean spiral:

$$\bar{r} = f(Re, R_m, L)\theta.$$

The variation of the orientation angle with the radius is in this case $\tan\varepsilon \propto 1/\bar{r}$, which shows that the curvature effect is expected to be important. Note that the inclination angle is positive, so the plotted patterns would correspond to type I instability.

7. Conclusion

The incompressible fluid flow in a rotor–stator configuration has been numerically investigated for cylindrical cavities ($R_m = 1$) with two aspect ratios $L = 2$ and $L = 5$ and for annular cavities of aspect ratio $L = 5$ with two values of the curvature parameter $R_m = 4$ and $R_m = 5$. The choice of the geometrical parameters and the efficiency of the three-dimensional pseudospectral method permitted the accurate investigation of the transition in both the Ekman and Bödewadt layers. For sufficiently high values of Re the base flow of Batchelor type becomes unstable to circular and spiral waves, as was found in the experimental work of Schouveiler *et al.* (1996, 1999). For the Bödewadt layer instability, computed values of the characteristic wave features (wavelength, spiral inclination angle, frequency and phase velocity) compare favourably with available measurements (Sirivat 1991; Savas 1987; Schouveiler 1999; Gauthier *et al.* 1999) and with axisymmetric numerical simulations (Cousin-Rittemard 1996; Lopez & Weidman 1996). In figure 15 the values of Re at which instability is observed in various numerical simulations and experiments are plotted as a function of $R_1/2h$. The combined numerical and experimental data show that all the instability configurations lie above the curve $Re(R_1/2h)^{1.8} = 10^4$. The patterns arising close to the rotating disc in the annular cavities also have characteristic parameters in good

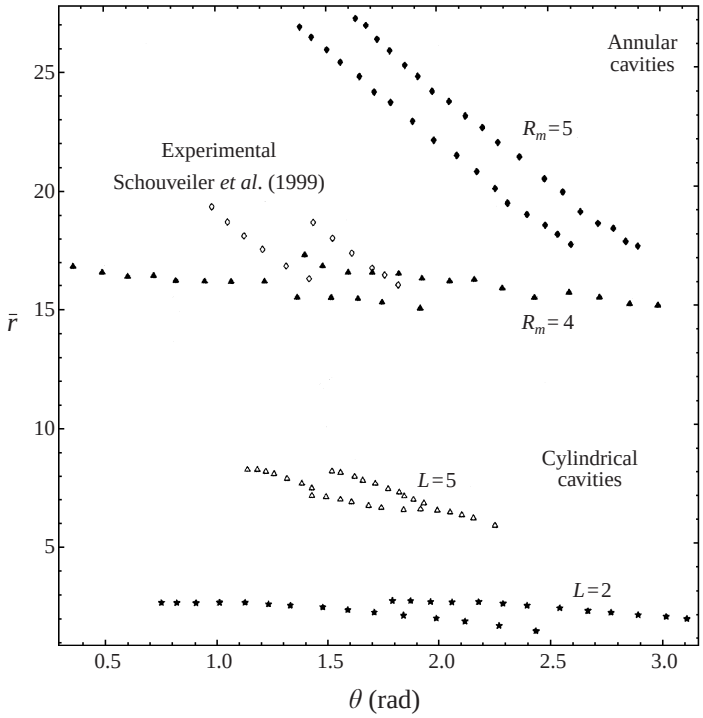

FIGURE 14. Display of two consecutive spiral arms of the Bödewadt layer in the plane $(\bar{r}, \theta)$ for different numerical and experimental cases. This view indicates a linear decrease of radius with the polar angle θ, characteristic of Archimedean spirals.

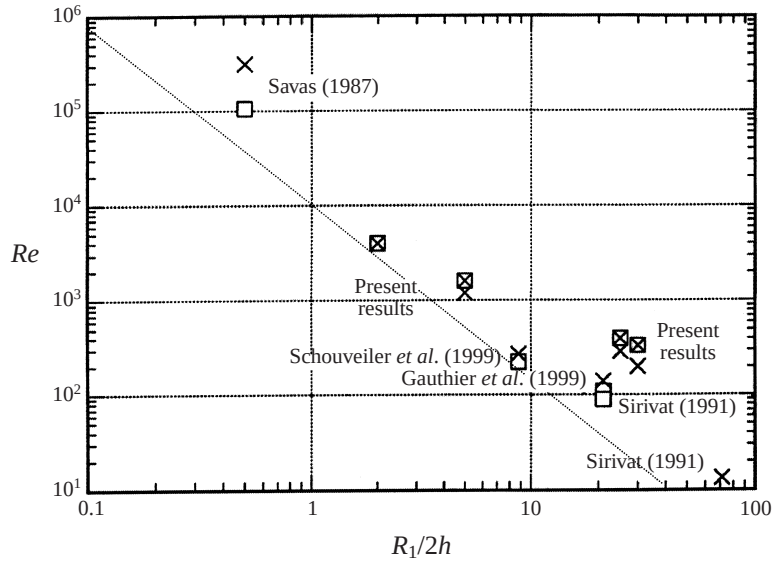

FIGURE 15. Diagram of various numerical and experimental results in the plane $(Re, R_1/2h)$. The blank squares indicate the axisymmetric structures and the crosses the three-dimensional spiral instability structures. The equation of the dashed line that gives a lower limit to transition is $Re(R_1/2h)^{1.8} = 10^4$.

agreement with the experimental measurements of the Ekman layer instability (Faller 1963; Caldwell & Van Atta 1970) and with our numerical study of the transition of the Ekman layer in a rotating cavity subjected to a radial forced flow (Serre *et al.* 2001).

The analysis and comparison with the literature on unstable flows indicate that the patterns observed in both boundary layers can be related to type I and type II instabilities. Two axisymmetric modes of standard type II have been observed in the form of circular structures. A stationary instability of the Bödewadt layer has been identified numerically, for the first time, far from the axis at $Re = 330$, $R_m = 5$. For higher rotation rates, an oscillatory mode appears in both boundary layers relatively close to the central axis for $Re = 400$, $R_m = 4$ and in the Bödewadt layer only in the near-axis region for $Re = 2000$, $L = 2$ and for $Re = 1600$, $L = 5$. This axisymmetric instability is robust and coexists with the three-dimensional spiral instability when the mean curvature is large, i.e. at small radii in the cylindrical cavity, when the radial confinement is sufficiently weak ($L = 5$). On the other hand, the axisymmetric instability is unstable to azimuthal disturbances when the curvature is small, i.e. at large radii in the annular cavity ($R_m = 5$). The evolved spiral structures are indicative of type I and type II instabilities and the number of spiral arms depends on the flow conditions. The three-dimensional spiral instability selected is unique, stable and independent of the magnitude and wavelength of the azimuthal disturbance. Structural defects in these three-dimensional patterns are also observed under certain conditions; these phenomena correspond to a variation of the wavelength involving a periodic structure of dislocations at a fixed radius around the circumference of the cavity. To our knowledge, this is the first time that dislocation phenomena have been reported when only spiral patterns are present.

Features of the axisymmetric and three-dimensional instabilities are found to be substantially different for small curvature at large radii, in the annular cavities ($R_m = 4$ and $R_m = 5$). We observed profound spatial and temporal variations as the axisymmetric circular waves underwent transition to spiral waves. Compared to the axisymmetric patterns, the three-dimensional ones do not exhibit the same strong disparity of roll size between the rotating and the stationary discs. The large difference in wavelengths between the rotating and the stationary disc layer disappear during the transient period and the wavelengths obtained in the final solution are comparable. Moreover, the magnitude of the fluctuation is nearly constant between the top and bottom layers. In contrast to the annular case, the instability wave characteristics $(\sigma, \varepsilon, \lambda)$ for the cylindrical cavity do not change appreciably; the three-dimensional flow retains properties close to the axisymmetric ones.

Our consideration of two cavities with different values of R_m and L permitted an exploration of phenomena affected by curvature and radial confinement. In particular, the instability regimes and the threshold values for the onset of instability are dependent on the local curvature. Moreover, the geometrical confinement is shown to have a strong effect on the dynamical behaviour in the cylindrical cavity: a pure Hopf bifurcation was observed for the smaller aspect ratio $L = 2$ while a transition from steady to non-periodic flow was found at $L = 5$. Confinement by the internal wall (shaft) was shown to have a profound effect on the amplification of the instabilities. For the annular cavity, the disturbance produced by the supercritical instability of the stator layer is transmitted along the shaft to the rotor and brings about a subcritical instability in the Ekman layer. For the cylindrical cavity, on the other hand, the unstable stator flow attenuates in the vicinity of the axis such that no subcritical Ekman instability of the Ekman layer on the rotor is observed. A study is in progress

on these aspects and into the convective/absolute transition in the Ekman layer (Lingwood 1996) in both the rotor–stator cavity and the open rotating cavity with throughflow.

Here, the effect of the curvature radius has been studied, in a relatively narrow range near the axis. However, important perspectives for future numerical work may be derived from the regime diagram of Schouveiler *et al.* (1996) and Schouveiler (1998). In particular, it would be interesting to study the flows at large distance from the axis the basic state for which involves a viscous flow with merged boundary layers. This regime evolves to non-periodic solutions as solitary waves and spots during the transition to turbulence. The numerical solitary vortex solution found by Hoffmann & Busse (2000) reinforces the expectancy of obtaining these unlocalized regimes. However the range of parameters for which the solitary vortex is stable has been determined neither experimentally nor theoretically. Thus, the numerical investigation seems to be feasible using cavities of large aspect ratio and at high values of the rotation rate. However, that study would be expensive in terms of CPU time.

The capability of the present numerical Navier–Stokes solver to represent complex three-dimensional flow structures in the whole cavity is very satisfying. All these results give us confidence that our direct numerical approach may be extended to simulate unsteady turbulent flows in the future.

The computations were carried out on a CRAY C98 and on a NEC SX5 from IDRIS/CNRS (Orsay). The authors acknowledge Professors P. D. Weidman, B. E. Launder and B. D. Shizgal for having carefully read the paper and making many useful suggestions. The authors are grateful to Professors R. Peyret (University of Nice), P. Le Quéré (LIMSI Paris) and J. P. Pulicani (University of Marseille) for fruitful discussions. The research was supported by the DGA (Dr Ormancey), Réseau MFN (CNRS-SPI) and the PICASSO Exchange Program. The authors also acknowledge financial support from DGICYT (Spain) with grants PB96-0148 and PB98-0074.

REFERENCES

Batchelor, G. K. 1951 Note on the class of solutions of Navier–Stokes equations representing steady rotationally-symmetric flow. *Q. J. Mech. Appl. Maths* **4**, 29–41.

Brady, J. F. & Durlofsky, L. 1986 On rotating disc flow. *J. Fluid Mech.* **175**, 363–394.

Buisine, D., Oble, F. & Andrianarahinjaka, H. 2000 Structures spirales à la périphérie d'une cavité interdisque. *C. R. Acad. Sci. Paris* **328**, 237–246.

Caldwell, D. R. & Van Atta, C. W. 1970 Characteristics of Ekman boundary layer instabilities. *J. Fluid Mech.* **44**, 79–95.

Canuto, C., Hussaini, M. Y., Quarteroni, A. & Zang, T. A. 1988 *Spectral Methods in Fluids Dynamics.* Springer.

Cherhabili, A. & Ehrenstein, U. 1995 Spatially localized two-dimensional finite-amplitude states in plane Couette flow. *Eur. J. Mech.* B/*Fluids* **14**, 677–696.

Cousin-Rittemard, N. 1996 Contribution à l'étude des instabilités des écoulements axisymétriques en cavité inter-disque de type rotor-stator. Doctorate Thesis, Université de Paris VI.

Cousin-Rittemard, N., Daube, O. & Le Quéré, P. 1998 Sur la nature de la première bifurcation des écoulements interdisques. *C. R. Acad. Sci. Paris* IIb **326**, 359–366.

Crespo del Arco, E., Maubert, P., Randriamampianina, A. & Bontoux, P. 1996 Spatio temporal behaviour in a rotating annulus with a source-sink flow. *J. Fluid Mech.* **32**, 1–27.

Daily, J. W. & Nece, R. E. 1960 Chamber dimension effects on induced flow and frictional resistance of enclosed rotating discs. *Trans. ASME: J. Basic Engng* **82**, 217–232.

Daube, O., Le Quéré, P., Cousin-Rittemard, N. & Jacques, R. 2001 Influence of curvature on transition to unsteadiness and chaos of rotor-stator disc flows. *J. Fluid Mech.* (submitted).

FALLER, A. J. 1963 An experimental study of the instability of the laminar Ekman boundary layer. *J. Fluid Mech.* **15**, 560–576.

FALLER, A. J. 1991 Instability and transition of the disturbed flow over a rotating disc. *J. Fluid Mech.* **230**, 245–269.

FALLER, A. J. & KAYLOR, R. E. 1966 Investigations of stability and transition in rotating boundary layers. In *Dynamics of Fluids and Plasmas*, pp. 309–329.

FOSTER, R. C. 1997 Structure and energetics of optimal Ekman layer perturbations. *J. Fluid Mech.* **333**, 97–123.

GAUTHIER, G., GONDRET, P. & RABAUD, M. 1999 Axisymmetric propagating vortices in the flow between a stationary and a rotating disc enclosed by a cylinder. *J. Fluid Mech.* **386**, 105–127

GOTTLIEB, D. & ORSZAG, S. A. 1977 *Numerical Analysis of Spectral Methods: Theory and Application.* SIAM, Philadelphia.

GRESHO, P. & SANI, R. L. 1987 On pressure boundary conditions for the incompresible Navier–Stokes equations. *Intl J. Numer. Meth. Fluids* **7**, 137.

GREENSPAN, D. 1972 Numerical studies of flow between rotating coaxial discs. *J. Inst. Maths Applics* **9**, 370–377.

GREENSPAN, H. P. 1969 *The Theory of Rotating Fluids.* Cambridge University Press.

HALDENWANG, P., LABROSSE, G., ABBOUDI, S. & DEVILLE, M. 1984 Chebyshev 3D spectral and 2D pseudospectral solvers for the Helmoltz Equation. *J. Comput. Phys.* **55**, 115–128.

HIDE, R. 1968 On source-sink flows stratified in a rotating annulus. *J. Fluid Mech.* **32**, 737–764.

HOFFMANN, N. & BUSSE, F. H. 2000 Isolated solitary vortex solutions for the Ekman-Couette layer. *Eur. J. Mech.* B/*Fluids* **19**, 391–402.

HOFFMANN, N., BUSSE, F. H. & CHEN, W. L. 1998 Transitions to complex flows in the Ekman-Couette layer. *J. Fluid Mech.* **366**, 311–331.

HOPFINGER, E. J. & LINDEN, P. F. 1990 The effect of background rotation in fluid motion: a report on Euromech 245. *J. Fluid Mech.* **211**, 417–435.

HUGUES, S. & RANDRIAMAMPIANINA, A. 1998 An improved projection scheme applied to pseudospectral methods for the incompressible Navier–Stokes equations. *Intl J. Numer. Meth. Fluids* **28**, 501–521.

HUGUES, S., SERRE, E., CRESPO DEL ARCO, E., RANDRIAMAMPIANINA, A. & BONTOUX, P. 1998 Instabilité tridimensionnelle de la couche d'Ekman dans une configuration annulaire avec flux forcé. *C. R. Acad. Sci.* IIb **326**, 873–879.

ITOH, M. 1991 On the stability of flow between coaxial rotating discs. In *Boundary Layer Stability and Transition to Turbulence. ASME FED*, vol. 114, pp. 83–89.

LILLY, D. K. 1966 On the instability of Ekman boundary flow. *J. Atmos. Sci.* **23**, 481–490.

LINGWOOD, R. J. 1995 Absolute instability of the boundary layer on a rotating disc. *J. Fluid Mech.* **299**, 17–33.

LINGWOOD, R. J. 1996 An experimental study of absolute instability of the rotating-disc boundary-layer flow. *J. Fluid Mech.* **314**, 373–405.

LINGWOOD, R. J. 1997 Absolute instability of the Ekman layer and related rotating flow. *J. Fluid Mech.* **331**, 405–428.

LOPEZ, J. M. 1996 Flow between a stationary and a rotating disc shrouded by a corotating cylinder. *Phys. Fluids* **8**, 2605–2613.

LOPEZ, J. M. & WEIDMAN, P. 1996 Stability of stationary endwall boundary layers during spin-down. *J. Fluid Mech.* **326**, 373–398.

MARLATT, S. W. & BIRINGEN, S. 1995 Numerical simulation of spatially evolving Ekman layer instability. *Phys. Fluids* **7**, 449–451.

MAUBERT, P., SCHIESTEL, R., ELENA, L., RANDRIAMAMPIANINA, A., CHAOUCHE, A. M., CRESPO DEL ARCO, E. & BONTOUX, P. 1993 Study of flow structure in rotating cavities: numerical predictions of laminar and turbulent, steady and unsteady flows. *AGARD* 23, pp. 1–23.

OWEN, J. M. & ROGERS, R. H. 1989 *Heat Transfer in Rotating Disk Systems, Vol. 1: Rotor-Stator Systems* (ed. W. D. Morris). Wiley.

OWEN, J. M. & ROGERS, R. H. 1995 *Heat Transfer in Rotating Disk Systems, Vol. 2: Rotating Cavities* (ed. W. D. Morris). Wiley.

PIKHTOV, S. V. & SMIRNOV, E. M. 1993 Boundary layer stability on a rotating disc with corotation of the surrounding fluid. *Fluid Dyn.* **27** (5), 657–663.

RANDRIAMAMPIANINA, A., ELENA, L., FONTAINE, J. P. & SCHIESTEL, R. 1997 Numerical prediction

of laminar, transitional and turbulent flows in shrouded rotor-stator systems. *Phys. Fluids* **9**, 1696–1712.

Raspo, I. 1996 Méthodes spectrales et de décomposition de domaine pour les ecoulements complexes confinés en rotation. Doctorate Thesis, Université de la Méditerranée, Marseille (France).

Reed, H. L. & Saric, W. S. 1989 Stability of the three-dimensional boundary layers. *Ann. Rev. Fluid Mech.* **21**, 235–284.

Rothman, E. 1991 Reducing round-off error in Chebyshev pseudospectral computations. In *High Performance Computing II* (ed. M. Durand & F. El Dabaghi), pp. 423–439. North Holland.

Rott, N. & Lewellen, W. S. 1966 Boundary layers and their interactions in rotating flows. *Prog. Aeronaut. Sci.* **7**, 111–144.

San'kov, P. I. & Smirnov, E. M. 1985 Bifurcation and transition to turbulene in the gap between rotating and stationary parallel disks. *Fluid Dyn.* **19**, 695–702.

San'kov, P. I. & Smirnov, E. M. 1991 Stability of viscous flow between rotating and stationary disks. *Fluid Dyn.* **26**, 857–864.

Savas, O. 1987 Stability of Bödewadt flow. *J. Fluid Mech.* **183**, 77–94.

Schouveiler, L. 1998 Sur les instabilités des écoulements entre un disque fixe et un disque en rotation. Doctorate Thesis, Université de la Méditerranée, Marseille (France).

Schouveiler, L., Le Gal, P., Chauve, M. P. & Takeda, Y. 1996 Experimental study of the stability of the flow between a rotating and a stationary disk. In *Advances in Turbulence VI* (ed. S. Gavrilakis *et al.*), pp. 385–388. Kluwer.

Schouveiler, L., Le Gal, P., Chauve, M. P. & Takeda Y. 1999 Spiral and Circular waves in the flow between a rotating and a stationary disc. *Expts. Fluids* **26**, 179–187.

Serre, E. 2000 Instabilités de couche limite dans des écoulements confinés en rotation. Simulation numérique directe par une méthode spectrale de comportements complexes. Doctorate Thesis, Université de la Méditerranée, Marseille (France).

Serre, E., Crespo del Arco, E. & Bontoux, P. 1999 Instabilité tridimensionnelle dans une cavité de type rotor-stator. *C. R. Acad. Sci. Paris* IIb **327**, 1139–1146.

Serre, E., Hugues, S., Crespo del Arco, E., Randriamampianina, A. & Bontoux, P. 2001 Spiral and circular instability patterns in an Ekman boundary layer flow. *Intl J. Heat Fluid Flows* **22**, 82–93.

Serre, E. & Pulicani, J. P. 2001 A 3D pseudospectral method for convection in a rotating cylinder. *Computers and Fluids* **30**(4).

Sirivat, A. 1991 Stability experiment of flow between a stationary and rotating disc. *Phys. Fluids* A **3**, 2664–2671.

Smith, N. H. 1947 Exploratory investigation of boundary layer oscillations on a rotating disc. *NACA Tech. Note* 1227.

Stewartson, K. 1953 On the flow between two rotating coaxial discs. *Proc. Camb. Phil. Soc.* **49**, 333–341.

Szeto, R. K. H. 1978 The flow between rotating coaxial discs. Doctorate Thesis, Caltech., Pasadena.

Vanel, J. M., Peyret, R. & Bontoux, P. 1986 A pseudospectral solution of vorticity-streamfunction equations using the influence matrix technique. In *Numerical Methods for Fluid Dynamics* (ed. K. W. Morton & M. J. Baines), pp. 463–475. Clarendon.

Weidman, P. D. 1976 On the spin-up and spin-down of a rotating fluid. Part 2. Measurements and stability. *J. Fluid Mech.* **77**, 709–735.